ISOCAM PSF REPORT

K. Okumura

June 26, 1998

version : 1.0

1 Introduction

The point spread function (PSF) of the ISOCAM is the results of the ISO telescope optics on one hand, and on the other hand, of the optical characteristics and the electronic behaviour of the camera.

Figs. 1 and 2 show the spatial sampling rates imposed by the pixel size for a single pointing image as a function of the lens. It is clearly seen that only LW3, LW7, LW8, LW9 and LW10 with 1.5 arcsec pixel-field-of-view (pfov) lens are correctly sampled. In order to improve the sampling rate, a micro scanning raster mode has been adopted in the PFS measurement. The minimum raster step size of ISO space craft is 2 arcsec. The maximum sampling rate is then one third of the pixel for 1.5, 3 and 6 arcsec pfov lenses. The sampling status using this micro scanning mode is listed in Tabs. 1 and 2.

The section 2 describes the calibration observations performed for PSF measurements. The section 3 describes the data analysis. The section 4 compares the measured PSFs with the ISO telescope optical model PSFs. The section 5 warns about possible ghost images in the CAM image, especially with a circular variable filter (CVF), which can not be separated from a point source. The section 6 gives an idea of the special use of the PSFs in the tentative deconvolution.

2 Observation mode and data processing of PSF measurements

In oreder to construct a set of PSFs, point sources giving high signal level in the linear regime have been selected among the list of calibration stars for each observing configuration. The fluxes of the calibration stars have been computed first based on the IRAS fluxes and K-band fluxes given by the ground based preparatory program and finally using the modelled spectral energy distribution computed by P.L. Hammersley. A micro raster observation mode has been adopted to minimize the pixel-to-pixel response variation of the detector and to obtain a better sampling rate. As this measurement requires a large number of observations and as the number of configurations to cover is large, the number of readouts is limited to 200 with readout frequence of 0.28 seconds.

The measurements have been made in micro scan mode with 6x6 raster for the lenses 1.5, 3 and 6 arcsec pfov. In order to get the best spatial sampling rate, the minimum step size of 2 arcsec has been used, except for 12 arcsec pfov lens, for which the step size of 3 arcsec has been used in a 4x4 raster. The source displaces then in a restricted zone on the detector depending on the lens used for the measurement (see Fig. 3). The micro scan allows to sample a point source

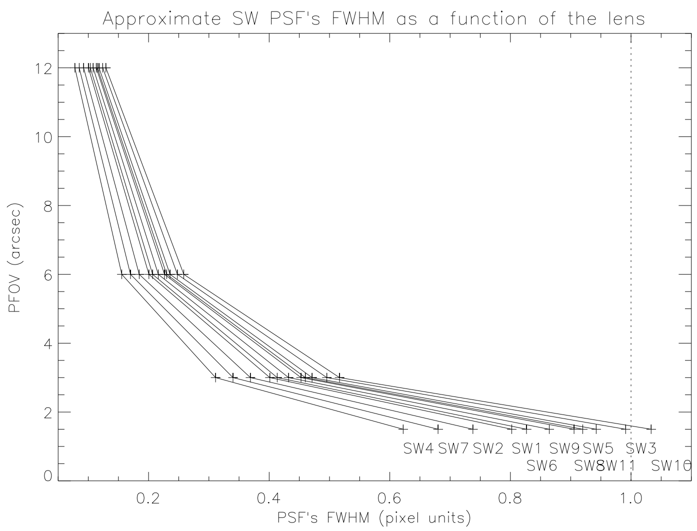

Figure 1: **Size of a point source with respect to the pixel size of SW channel**

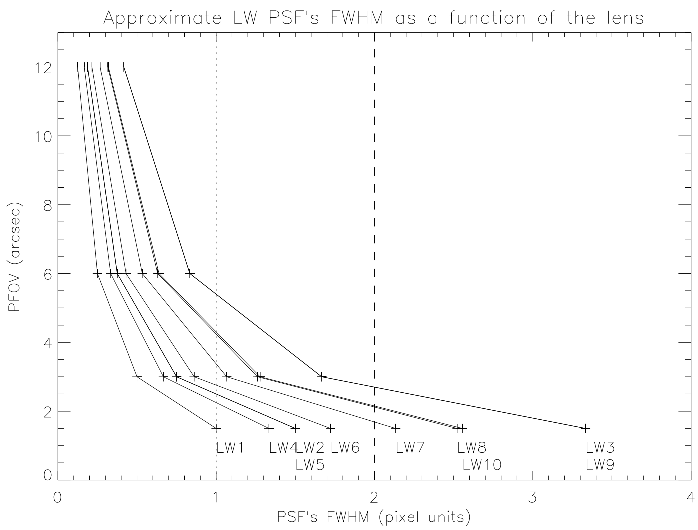

Figure 2: **Size of a point source with respect to the pixel size of LW channel**

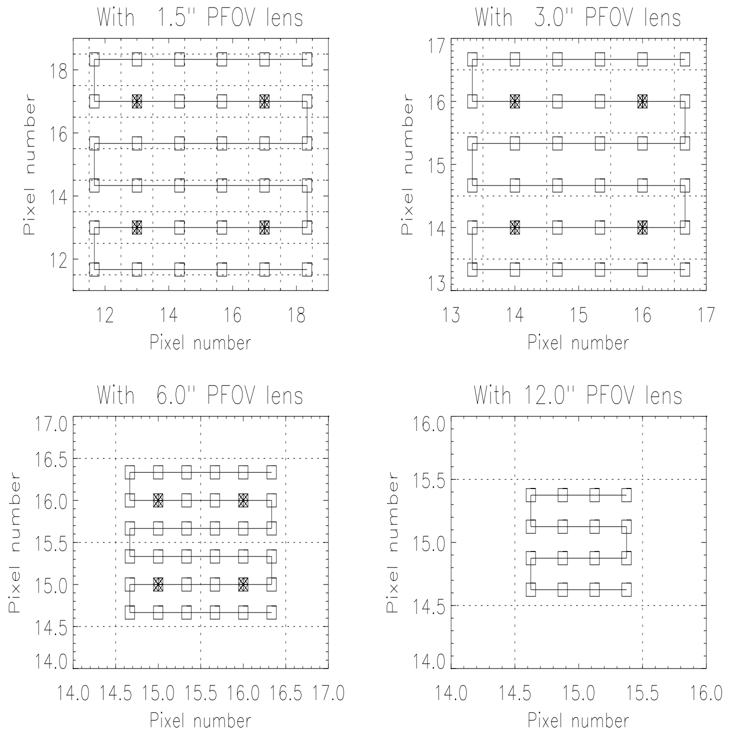

Figure 3: **Point source displacement along a scanning raster**

image by one third of the pixel size for 1.5, 3 and 6 arcsec pfov lenses, and by one quarter for 12 arcsec pfov lens. The 12 arcsec pfov gives a very small point source image with respect to the pixel size and the PSF measurements are also supposed to give a responsivity map of one pixel.

In order to investigate a spatial variation of PSFs on the detector array, some measurements have been made by putting a point source on different points of the array using LW7 filter for 1.5, 3 and 6 arcsec pfov and using LW1 for 12 arcsec pfov (see Figs. 4 to 6). Some off-source measurements are also made as shown below.

2 off-source staring measurements
First central PSF raster measurement
Off-centered PSF raster measurement
Off-centered PSF raster measurement
...
Last central PSF raster measurement
2 off-source staring measurements

All the PSF measurements performed are presented in Tab. 3.

Tabs. 1 and 2 list the sampling status for the raster observations of PSF measurements.

2.1 Reduction of PSF data for calibration files

The standard reduction procedure was applied to the sets of PSF measurements:

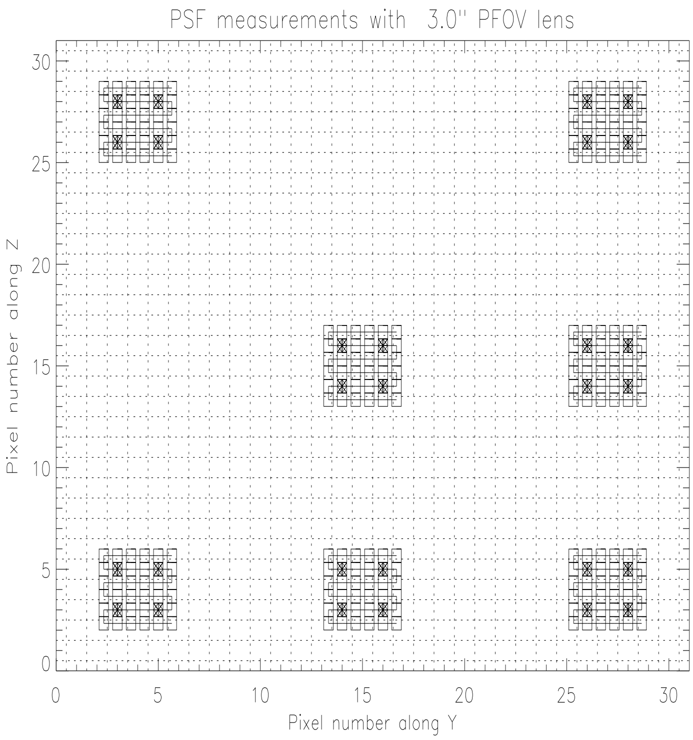

Figure 4: PSF measurements on different positions on the detector

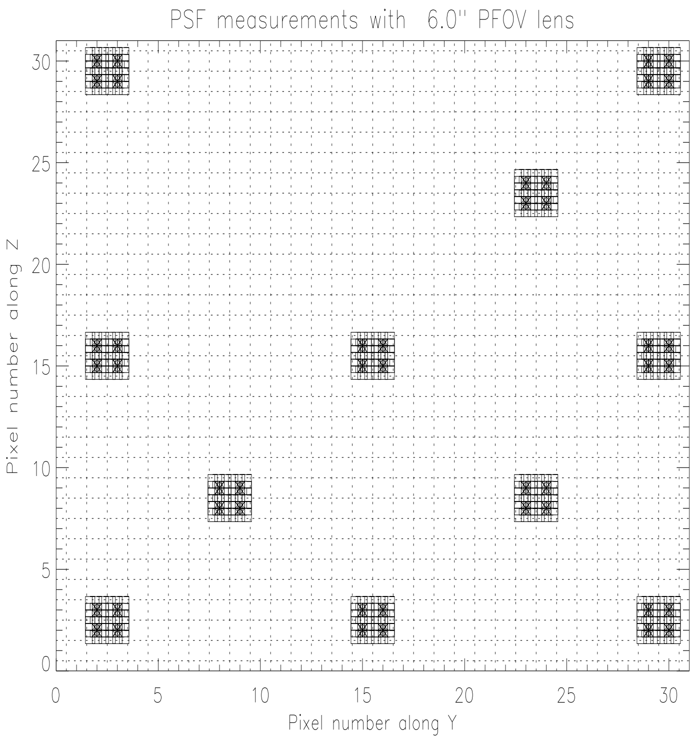

Figure 5: PSF measurements on different positions on the detector

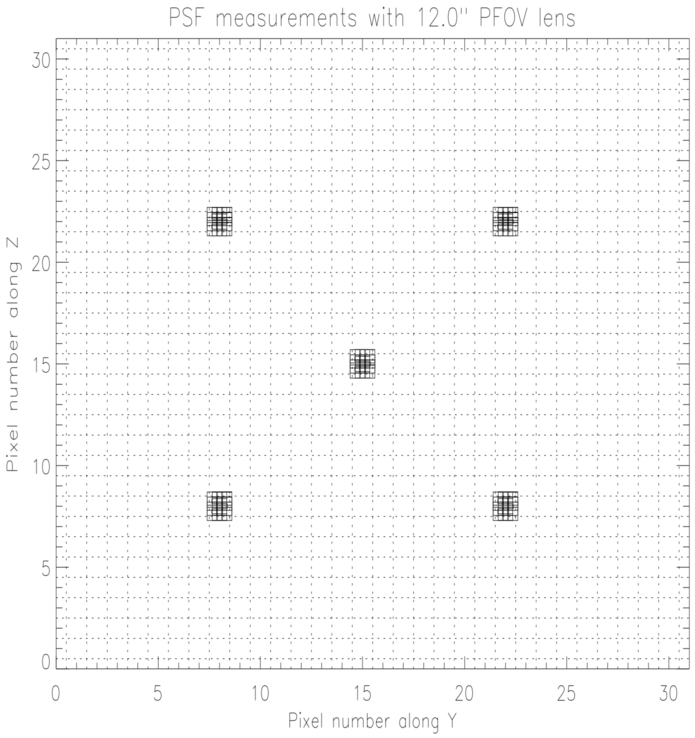

Figure 6: PSF measurements on different positions on the detector

Table 1: SW PSF sampling, y : well sampled, n : badly sampled

pfov	SW1	SW2	SW3	SW4	SW5	SW6	SW7	SW8	SW9	SW10	SW11
1.5	y	y	y	y(n)	y	y	y	y	y	y	y
3	n	n	n	n	n	n	n	n	n	n	n
6	n	n	n	n	n	n	n	n	n	n	n
12	n	n	n	n	n	n	n	n	n	n	n

Table 2: LW PSF sampling, y : well sampled, n : badly sampled, y(n) : critically sampled

pfov	LW1	LW2	LW3	LW4	LW5	LW6	LW7	LW8	LW9	LW10
1.5	y	y	y	y	y	y	y	y	y	y
3	n	y	y	n	y	y	y	y	y	y
6	n	n	y	n	n	n	n	y(n)	y	y(n)
12	n	n	n	n	n	n	n	n	n	n

Table 3: Performed PSF measurements

Filter	Lens	TDT No.	Positions	Target	Tint	comments
lw1	1.5	038031-32	1	HIC69713	0.28	very faint spider
lw1	3	038018-19	1	HIC89474	0.28	no arc seen
lw1	3	042046-47	1	HIC89474	0.28	no arc seen
lw1	6	038022-23	1	HIC77277	0.28	faint ghost
lw1	12	038026-27	1	HIC69713	0.28	near col.24, double star
lw1	12	038052-61	6	HIC69713	0.28	ghost, double star
lw1	12	244062-71	6	HIC69107	0.28	
lw2	1.5	Rev.100	1	HIC87833	0.28	killed by a saturation
lw2	1.5	140003-04	1	HIC92782	0.28	low level off-centered
lw2	1.5	846025-27	1	OH IR	0.28	cold PSF not included in Cal-g
lw2	3	119040-41	1	HIC77760	0.28	spider
lw2	6	093044-45	1	HIC80331	0.28	saturated with strong ghost
lw2	6	133046-47	1	HIC96441	0.28	ghost
lw2	6	342004-05	1	HIC85317	2.10	3x3 raster
lw3	1.5	100018-19	1	HIC87833	0.28	switched from lw2 saturation
lw3	1.5	119034-35	1	HIC80331	0.28	well seen arcs
lw3	1.5	510005-07	1	OH IR	0.28	cold PSF not included in Cal-g
lw3	3	119036-37	1	HIC80331	0.28	spider and arcs
lw3	3	342008-09	1	HIC98962	2.10	3x3 raster
lw3	3	426024-32	5	HIC98962	2.10	6x3 raster
lw3	6	119038-39	1	HIC74083	0.28	very faint ghost
lw3	6	201005-08	2	HIC78527	0.28	
lw3	6	342006-07	1	HIC96441	2.10	3x3 raster
lw3	12	244036-45	6	HIC77760	0.28	
lw4	1.5	189005-06	1	HIC78542	0.28	
lw4	3	182012-13	1	HIC78542	0.28	
lw4	6	300005-06	1	HIC78542	0.28	
lw5	1.5	175035,37	1	HIC84835	0.28	backgrnd failed
lw5	3	503022-24	1	HIC96441	2.10	
lw5	6	300007-08	1	HIC84835	0.28	
lw6	1.5	244049-50	1	HIC92782	0.28	
lw6	3	272027-28	1	HIC92782	0.28	unretrievable
lw6	3	510010-12	1	HIC101245	2.10	
lw6	6	272029-30	1	HIC92782	0.28	
lw7	1.5	014022-23	1	HIC92782	2.10	Tint=15
lw7	1.5	014027-28	1	HIC92782	0.28	failed
lw7	1.5	038033-34	1	HIC92782	0.28	faint arcs
lw7	3	038037-48	8	HIC70791	0.28	very faint tripod
lw7	6	042030-45	12	HIC74083	0.28	some ghost
lw8	1.5	175029-30	1	HIC87585	0.28	
lw8	3	189013-14	1	HIC87585	0.28	
lw8	6	189015-16	1	HIC87585	0.28	
lw9	1.5	038035-36	1	HIC87833	0.28	beautiful arcs
lw9	1.5	223004-05	1	HIC73005	2.10	
lw9	1.5	307018-19	1	HIC94779	2.10	3x3 raster
lw9	1.5	307020-21	1	HIC87585	2.10	3x3 raster
lw9	1.5	307024-25	1	HIC80331	2.10	3x3 raster
lw9	1.5	307022-23	1	HIC87585	2.10	3x3 raster
lw9	1.5	307016-17	1	HIC94376	2.10	3x3 raster
lw9	1.5	501042-45	2	HIC94376	2.10	6x3 raster
lw9	3	067013-14	1	HIC80331	0.28	spider and arcs
lw9	6	038024-25	1	HIC80331	0.28	ghost at bottom
lw9	6	133055-56	1	HIC80331	0.28	ghost at bottom
lw10	1.5	300003-04	1	HIC78527	0.28	
lw10	3	189007-08	1	HIC78527	0.28	
lw10	6	196005-06	1	HIC78527	0.28	killed by earth seeing accident
lw10	6	272031-32	1	HIC78527	0.28	
lw10	6	363008-10	1	HIC77277	2.10	3x3 raster
CVF	3	433008-10	1	HIC77760	2.10	6.221 μm
CVF	3	433011-13	1	HIC77760	2.10	8.379 μm
CVF	3	433014-16	1	HIC77760	2.10	10.52 μm
CVF	3	433003-05	1	HIC67459	2.10	15.0 μm
CVF	6	440015-17	1	HIC77760	2.10	6.221 μm
CVF	6	440018-20	1	HIC77760	2.10	8.379 μm
CVF	6	440012-14	1	HIC78276	2.10	10.52 μm
CVF	6	440005-07	1	HIC67459	2.10	15.0 μm
sw1	12	054004-11	6	HIC77760	0.28	faint ghost?
sw5	1.5	014025-26	1	HIC69713	2.10	Tint=15, double star
sw5	1.5	038028-29	1	HIC74083	0.28	doble star?
sw5	1.5	066032-33	1	HIC69713	0.28	Tint=2, double star
sw5	3	042018-27	8	HIC69713	0.28	double star (companion at 15 pix)
sw5	3	363002-04	1	HIC73005	2.10	3x3 raster
sw5	6	046049-62	12	HIC69713	0.28	double star (companion at 8 pix)
sw5	6	363005-07	1	HIC73005	2.10	3x3 raster
sw5	6	524034-35	1	HIC85317	2.10	6x3 raster
sw5	12	475032-33	1	HIC85317	2.10	6x3 raster

- Deglitching
- Scale gain to one
- On-board processing check (normal or accumulated)
- Stabilised part estimation
- Average frames on the stabilised part
- Dark subtraction
- Detector flatfield correction
- Optical flatfield correction

The temporal deglitching method was used to minimize accidental point source flux loss due to some other deglitching methods. For the stabilization estimation, sigma clipping method was adopted bearing in mind that this does not extrapolate unstabilized pixel values but takes only the values of the last frame.

Then PSF measurement specific processing are applied:

- Determination of the point source position on the detector
- Average over in-pixel equivalent measurements
- Normalise PSFs of one configuration with respect to one PSF

With the assumption that the spatial variation of PSF is small on the zone of micro scan, the measurements are grouped by their location in the pixel except for 12 arcsec lens measurement whose micro scanning zone does not extend over one pixel. This gives 9 groups of 4 members (in-pixel equivalent measurements) out of 36 raster points. The 4 members of each group are then averaged to make a "mean PSF" of the averaged location of these members on the array. In this way 9 PSFs are generated out of one raster measurement, except for 12 arcsec pfov measurement which gives directly 16 PSFs. The averaging 4 measurements also allows to get rid of the lack of the column 24 in a single image.

3 Obtained data and analysese

3.1 Determination of the point source position on the detector array

The absolute position of the point source in pixel coordinates is determined by IDL CNTRD routine or a barycentre routine (when the former fails). Any position determination method applied to an individual point source image gives a biased result for the under-sampled data; the worse sampled are the data, the more centered on a pixel is the resulting postion (see section 6). Fig. 7 shows an example of biased result of position determination.

By taking into account the *a priori* raster pattern, this bias can be corrected to some extent and the point sorce position estimation can be improved up to a fraction of the pixel size.

Three different methods have been used to refine the point source position estimate by taking the raster pattern into account.

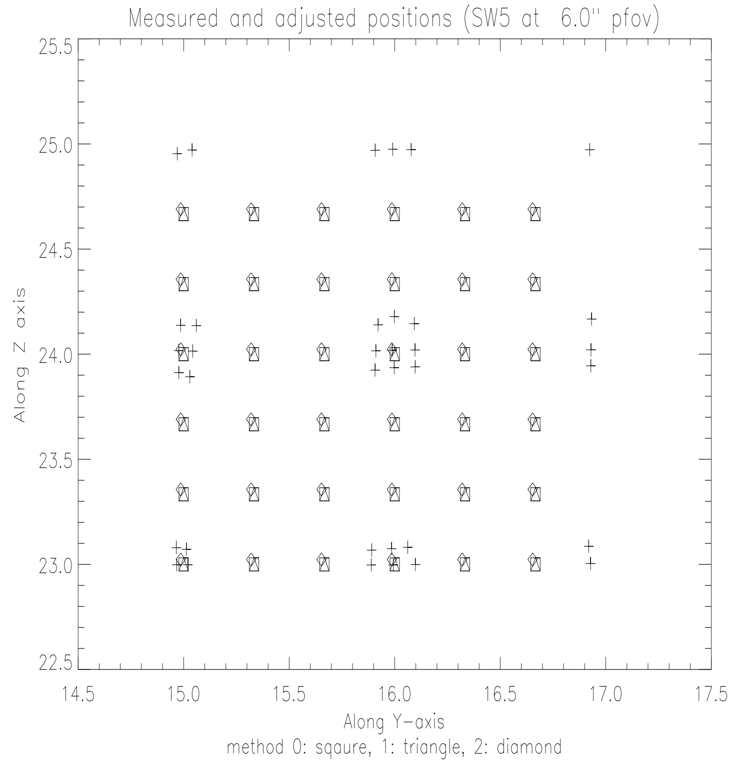

Figure 7: **Any position determination method applied to an under-sampled individual point source image gives an biased result: position is pulled towards the centre of a pixel.**

Method 0:	A set of equivalent PSFs whose first position estimate gives the closest to the center of a pixel is considered as “centered” on the pixel. The positions of the other raster points are computed following the raster pattern.
Method 1:	The position of the brightest pixel should move in a determined way according to the position of the start point. This fact allows to determine the positions up to the sampling rate in the pixel.
Method 2:	Simple least square method fitting the ideal raster pattern on the first position estimate.

The first two methods give an accuracy of the pixel sampling rate, whereas the method 2 can give a more accurate result.

Method 2:

A least square method without imposing any *a priori* discrete values on the fractions of pixel gives sometimes a more convincing result. The Fig. 8 shows one of those examples. The method 0 and the method 1 give different results in this example; the former gives a raster pattern shifted by one raster step size in the I-axis direction with respect to the latter. However, the individual position estimates (plus signs) seem to suggest that neither of them is appropriate. For example, these first estimates for the 3 vertical alignments on the left side of the raster indicate that all of them lie only on one pixel alignment I=[1.5, 2.5], whereas the method 0 (square signs) gives only 2 alignments. The method 1 (triangle signs) gives 3 alignments in this range, but the first estimates should then have given 3 alignments with equal distance as seen in Fig. 7, which is not the case. One can suspect that the real raster pattern is located slightly

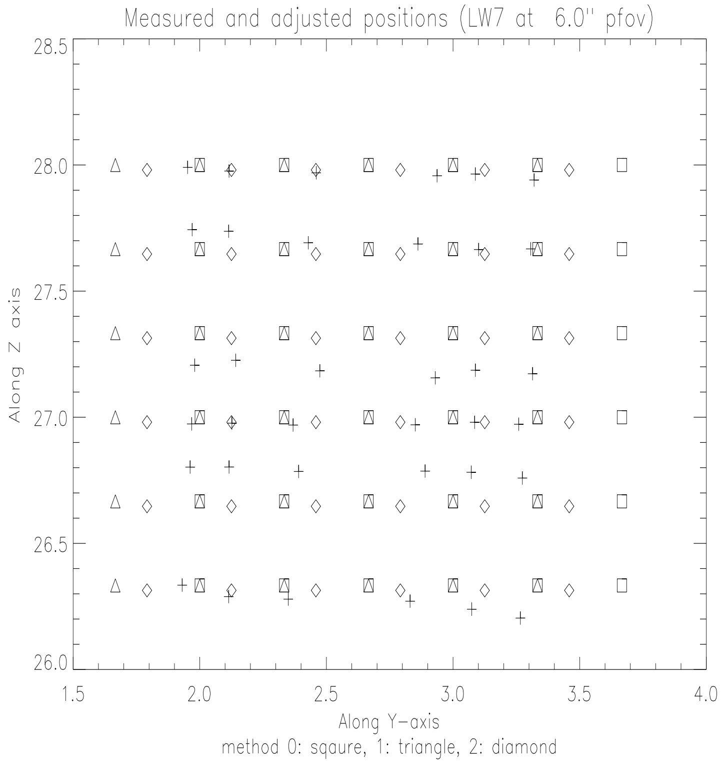

Figure 8: **A least square method gives estimate values of the point source positions**

to the right because of the asymetrical distant alignments. This result is obtained only by the method 2 (diamond signs). The PSF Cal-G files since version 4 has been produced using this method.

3.2 Stability of the PSF measurements

Fig. 9 shows an example of stability for a SW PSF measurement. The 5 curves represent from the top: mean value over the image, median value over the image, median value subtracted mean value, horizontal pixel coordinate and vertical coordinate. This example is taken from the configuration 1.5 arcsec pfov at SW5 filter in the revolution 38 (Dec. 25th 1995) which had no off-source measurements before, so that the SW detector was put into prime instrument just at the beginning of this observation. The telescope stays at each raster point during 56 seconds. The stabilisation time required after the SW prime uplink to a reasonable level is estimated to be about 20 to 30 minutes. This can be seen in the evolution of median values over the raster sequence which decreases from 3.5 to 0.5 ADU/s/gain. This SW5 PSF measurement will not be able to be processed within a reasonable error unless a valid stabilization routine is applied. The actual version of PSF Cal-G file contains the PSFs by the standard processing shown in the section 2.1. Therefore, the major error arises mainly from the unsufficient stabilization correction in this case.

Fig. 10 shows an example of stability for a LW PSF measurement. The 5 curves have the same signification as the previous figure. This measurement has been made for the configuration 1.5 arcsec pfov at LW7 filter right after a background measurement at LW1 with 1.5 arcsec pfov. This time, the meadian values increases over the raster sequence. This represents a very slow stabilization of the faint background flux which is higher at LW7 than at LW1 filter. The

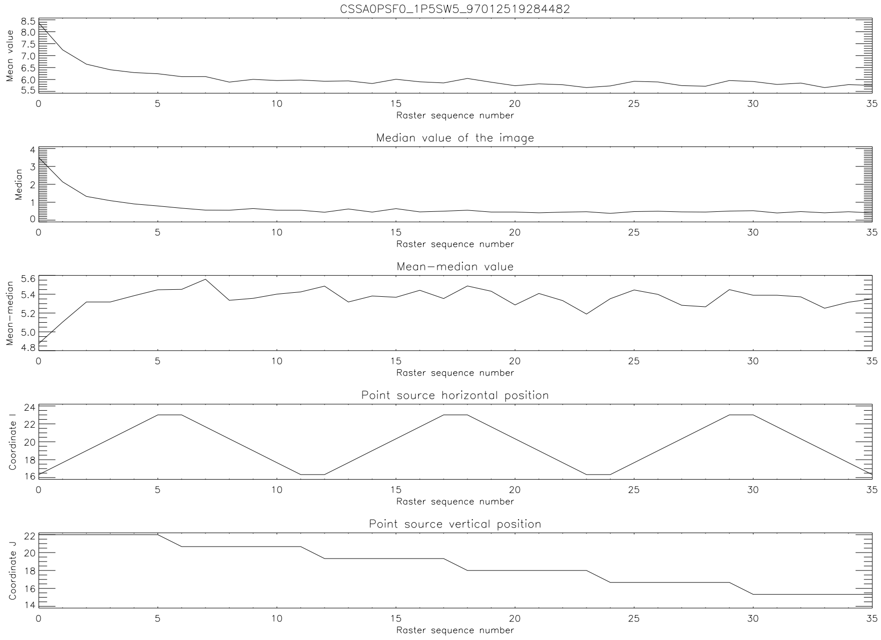

Figure 9: First 10 raster points are clearly not stabilized yet.

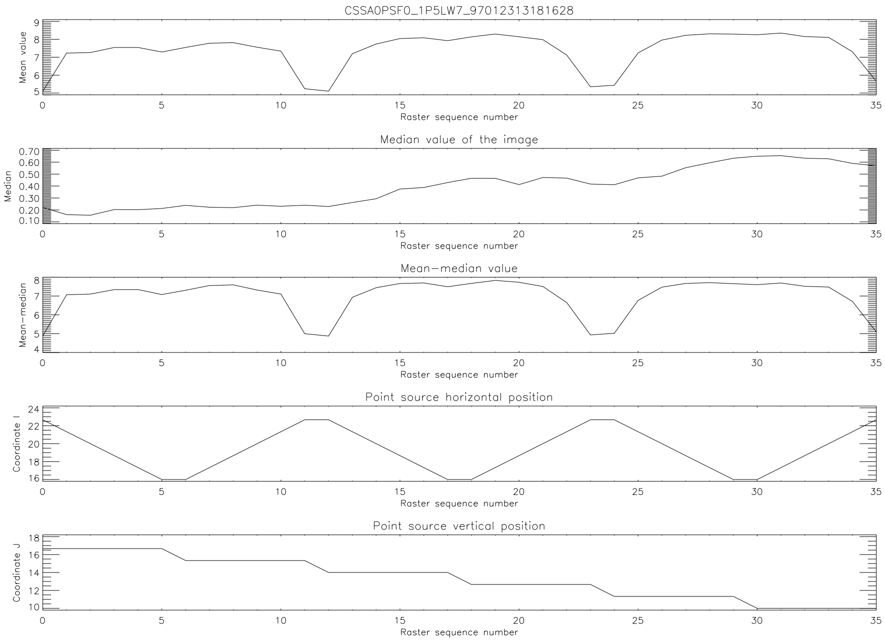

Figure 10: A very slow stabilization of the weak background flux is seen over the whole raster sequence

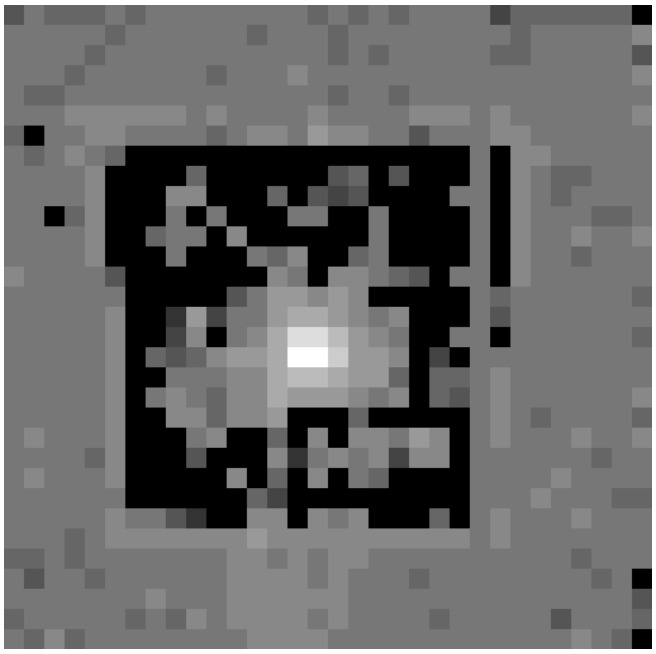

Figure 11: After the standard processing, the background level is lower than the dark current level which can be seen outside the field mirror

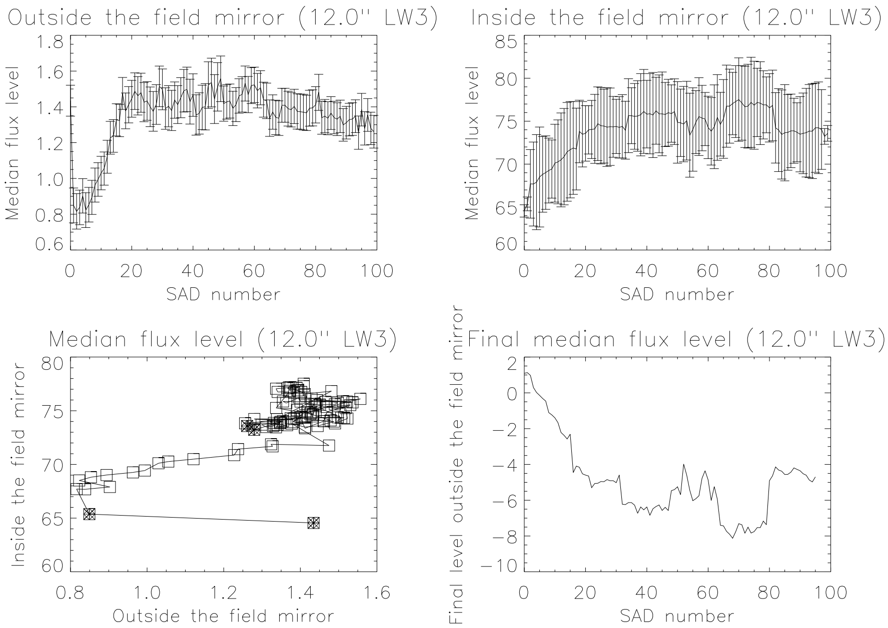

Figure 12: Evolution of inside and outside of the Fabry field mirror over the whole PSF measuement sequence for 12 arcsec pfov are LW3 filter.

variation is however relatively small (0.4 ADU/s/gain). The periodical drops seen in the mean values are caused by the target point source falling on the dead column (column 24), which is clearly seen in the horizontal pixel coordinate curve.

The amplitude of the background level variation due to the stabilization depend on the difference of the background flux between the actual and previous configuration. The error due to the stabilization can be dicreased by a long enough off-source observation before the on-source observation, but the best way is, of course, to correct for the stabilization beyond each raster point period.

Fig. 11 is an example of a curious result caused by the stabilization problem after the standard processing. This measurement has been performed with 12 arcsec pfov at LW3 filter in the revolution 244. When using the 12 arcsec lens the field mirror is smaller than the detector size and its edges are seen if the background level is detectable which is the case for LW3 filter. The image shows a background level inside the field mirror lower than the diffuse stray light affected dark current level. Inside the field mirror, the background level rises slowly from about 65 to 73 ADU/s/gain over all the raster sequence whereas the flux level outside the Fabry mirror arises very little (this is an indication of a diffuse stray light: see the section 5). Fig. 12 shows these flux level evolution. Some images at the beginning of the sequence result then in a negative background level after the background subtraction.

When all the rasters of one configuration are processed by the CFDP (Calibration File Derivation Procedure) using the point source determination method 0 or 1, the procedure takes, by default, the first PSF raster as the central PSF set and not the last one. This is because the calibration file does not accept redundant data (same point source positions). If the method 2 is used, then the first central PSF set can take different point source positions than the last PSF set, therefore both of them can be included in the calibration file. As the PSF Cal-G files up to the version 3.4 have been generated using the method 0 or 1, only the last central PSF set has been included in order to give more stabilized data sets.

3.3 Normalization factor and the average of equivalent PSFs

For a PSF measurement with a point source placed at the centre of the detector array, all the PSFs are normalized by the integrated signal value of the PSF having integer pixel coordinates values. This normalization is aimed to give a photometric correction as a function of position in the pixel. For a PSF measurement in a zone at the edge of the detector array, normalization is done with respect to the PSF of the central zone of the detector of the same configuration. This normalization allows to add an occasional vignetting correction for the point source photometry. The integrated signal value is computed by the aperture photometry method, because the background subtraction does not allow to define a good zero level. Unfortunately this method underestimates the integrated value especially for large PSFs, as their low level extends outside the detector array.

Generally the normalisation factor varies about 2% to 3% around the unity. However this variation does not seem to reflect the responsivity difference on one pixel: 4 PSFs with the same positin on a pixel show the same order of dispersion. The PSFs with 12 arcsec pfov show a larger dispersion (up to 40%) between different locations on the detector array. This large value comes from a bad accuracy of signal integration caused by the ghost and probably from the remaining vignetting effect after the flat field correction.

Figs. 13 and 14 shows the flux evolution over the whole sequence of rasters of PSF measurements together with the rms over each rastrer and pixel coordinates of the point sorce. The periodic flux drops seen in Fig. 13 from the image sequence number 150 to 250 are due to the

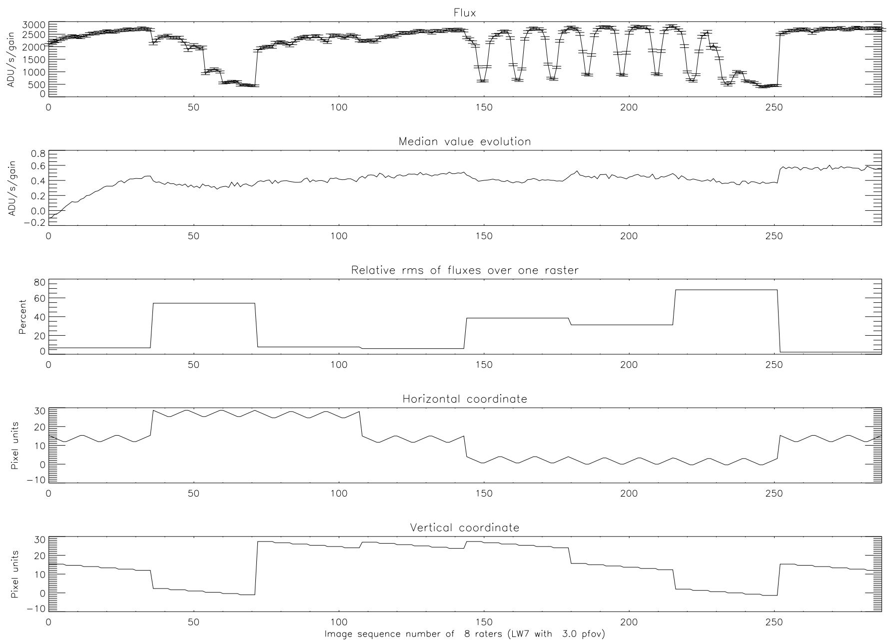

Figure 13: Evolution of the flux level over the whole sequence of rasters of PSF measurements with 3 arcsec pfov at LW7 filter

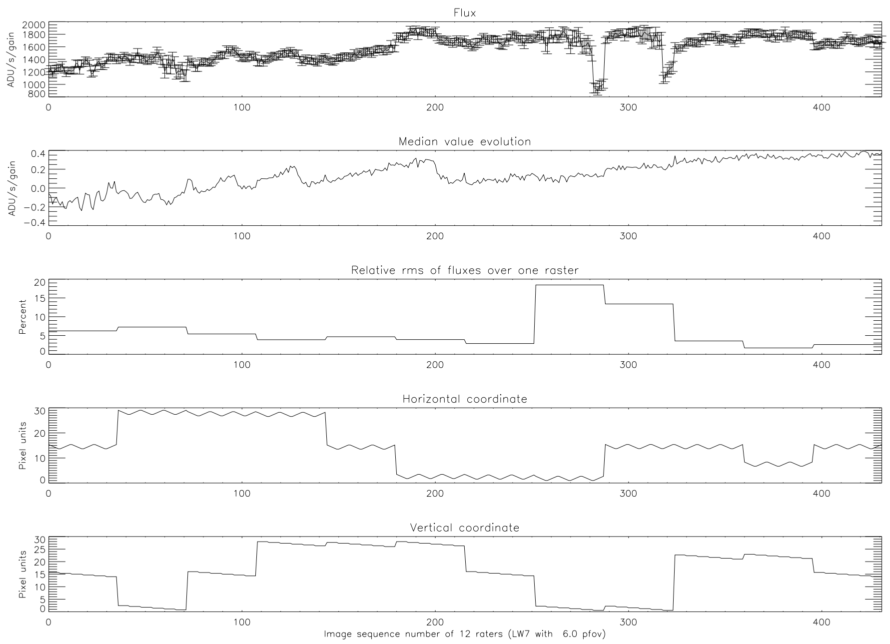

Figure 14: Evolution of the flux level over the whole sequence of rasters of PSF measurements with 6 arcsec pfov at LW7 filter

target source fallen too close to or even outside the Fabry field mirror, which can be seen in the horizontal coordinate of the point source moving periodically to zero in the raster scan. This flux drop is sometimes modulated by another long term periodic flux fall, when the vertical coordinate of the source approaches the field mirror edge (vertical coordinate gives only one period on one raster sequence). This is seen around the image sequence number 70 and 250.

In order to account for the flux loss on the field mirror edge, all the PSF measurements are normalized by the same factor corresponding to the flux of the point source located most near a pixel centre and placed on the centre of the detector. This normalization allows to take account of the flux variation over the detector, however the long term transient effect can cause an error on this flux variation. The median value indicates approximately the low level flux evolution of the image. The fluxes in the first raster are clearly affected by the transient. Rasters which has no flux loss on the field mirror edge in this measurements are only the first and the last ones. The last raster shows the flux dispersion of about 3%, whereas the dispersion of the first raster is larger (8%) because of the transient effect.

The PSF measurements with 6 arcsec lens shown in Fig. 14 have more rasters without flux loss on the detector edge. Obvious flux loss is seen around the image No. 285 and 320 due to the vertical coordinate of the point source reaching zero value. Apart from these flux loss, no obvious correlation is seen between the flux evolution and the point source position. On the contrary, one can see the rise of the low flux level in the median value.

In the present state the transient correction over the whole set of rasters is not applied. In order to minimize the error due to the transient effect, a second background correction is applied before the average of equivalent PSFs and the normalization factor is computed in the averaged set of PSFs.

As the transient causes a major difficulty, a new observation mode of PSF measurements was elaborated and used after the PV phase. The main modification consists of measuring longer at each raster points to obtain a better stabilization at faint flux level. The raster size is reduced to 3×3 or 6×3 to maintain well sampled observation within a reasonable duration. The readout frequency is taken to be 2.1 seconds as a large fraction of science obsrvations in the mission data base.

The relative pointing error on each raster point can cause a degradation rather than an improvement of the PSF when averaging these equivalent PSFs especially for those with 1.5 arcsec pfov. Some improvement has been investigated for the purpose of deconvolution. But it turned out that the processing should go back to the frame level to take account of the pointing jitter (see section 6). This aproach requires to examine all the individual frames of the PSF measurement, and so requires a large amount of data storage. Therefore, it has been decided to keep the averaged PSF in the Cal-G files.

4 Comparison with theoretical PSFs

4.1 Optical PSF computation

The primary mirror of the ISO telescope has a diameter of 634 mm but the entrance pupil diameter D of the telescope is determined by the combination of the primary and the secondary mirror to give 600 mm.

In the optical PSF model computation, the pupil image is created in the Fourier space. The pixel size $P_{Fourier}$ in this space is given by:

$$P_{Fourier} = \frac{\lambda}{SP_{rad}}$$

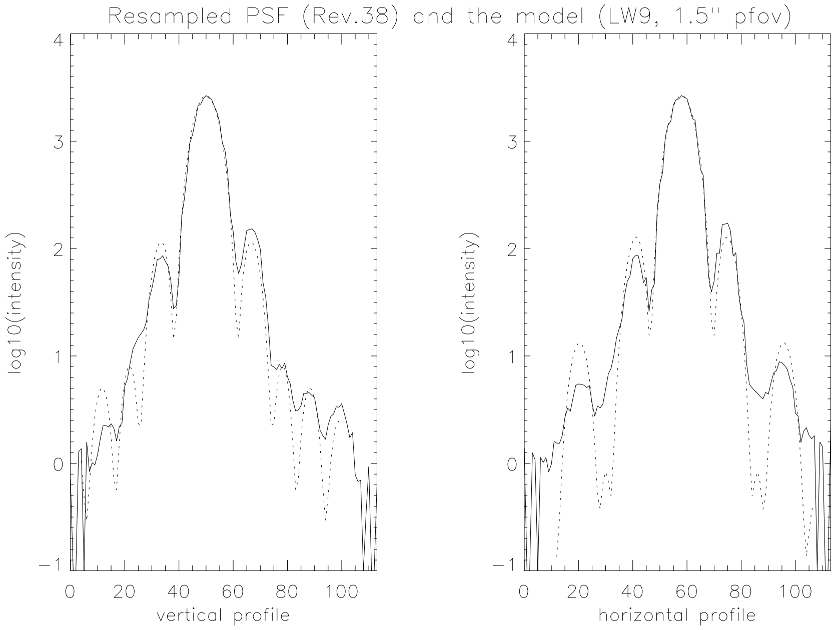

Figure 15: **Comparison of measured PSF and modelled PSF with LW9 and 1.5 arcsec pfov**

where λ is the typical wavelength of the bandpass of the used filter, S is the size of the considered image expressed by the number of pixels (the image should be square) and P_{rad} is the pixel size of the image in the direct space in radian. The diameter Δ of the circular aperture in the Fourier space in pixel units is then given by dividing the telescope diameter D by the pixel size $P_{Fourier}$:

$$\Delta = \frac{D}{P_{Fourier}} = \frac{D}{\lambda} S P_{rad}$$

If λ is expressed in μm, its radius is given by:

$$R = \frac{\Delta}{2} = \frac{0.6 \cdot 10^6}{2P_{Fourier}} = \frac{0.3 \cdot 10^6 S P_{rad}}{\lambda} \tag{1}$$

In order to operate in a correctly sampled computation both in the Fourier and in the direct space, it is necessary to create a finer sampling and a larger image size than the real image coming from ISOCAM detectors. If, in addition, one wants to add the detector pixel convolution effect on the optical PSF model, then the sampling in the direct space should be better than at least a half of the pixel size.

Once the image size is chosen, the central obscuration and the tripod structure are added to the main aperture by respecting their proportion of size. The Fourier transform of the aperture then gives the optical PSF which will be convolved by the detector pixel size and resized to the real size of a detector array. For more correct models, one should integrate on the bandpass profile of each filter multiplied by the spectral energy distribution of the source. However, the monochromatic PSF is well compared with the data as long as the bandpass is small. We first use here the model without taking into account the bandpass integration effect.

4.2 Comparison with the data

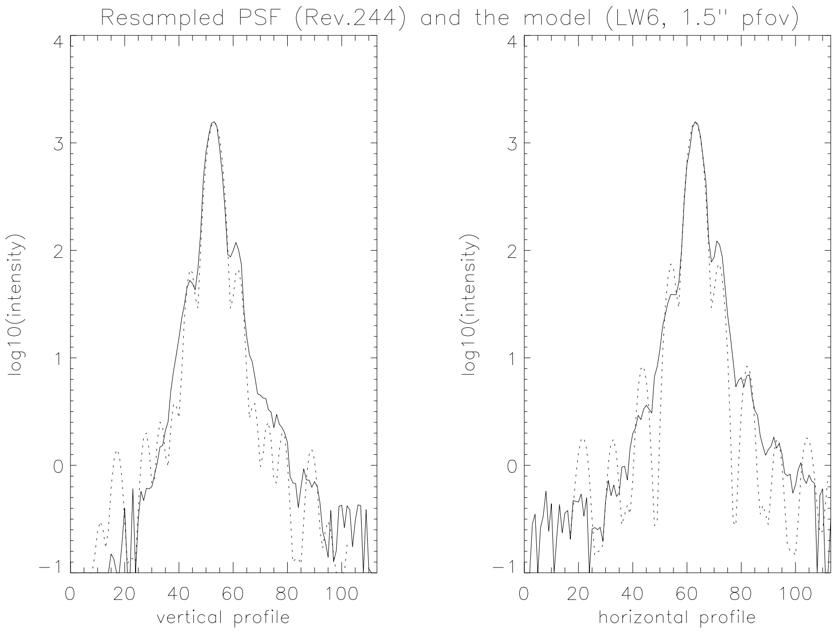

Figure 16: Comparison of measured PSF and modelled PSF with LW6 and 1.5 arcsec pfov

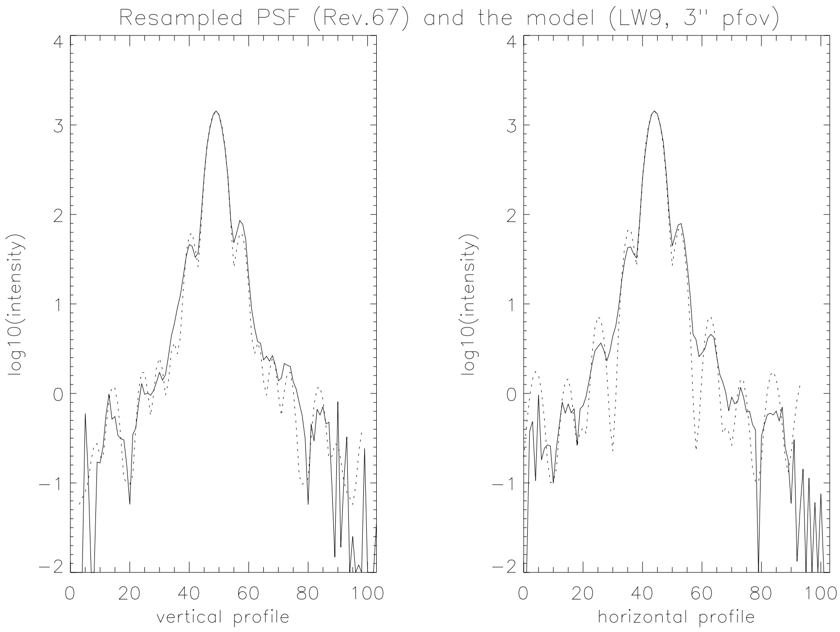

Figure 17: Comparison of measured PSF and modelled PSF with LW9 and 3 arcsec pfov

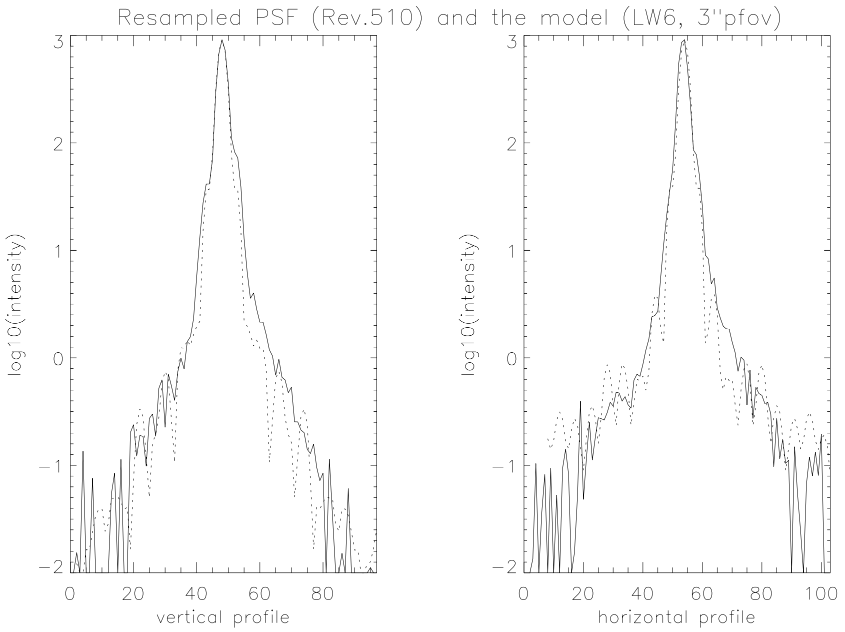

Figure 18: Comparison of measured PSF and modelled PSF with LW6 and 3 arcsec pfov

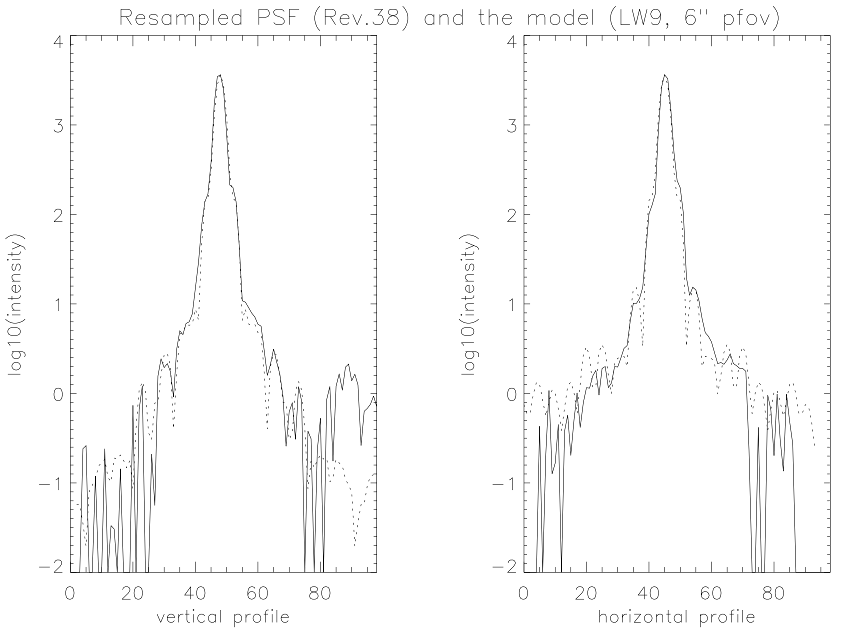

Figure 19: Comparison of measured PSF and modelled PSF with LW9 and 6 arcsec pfov

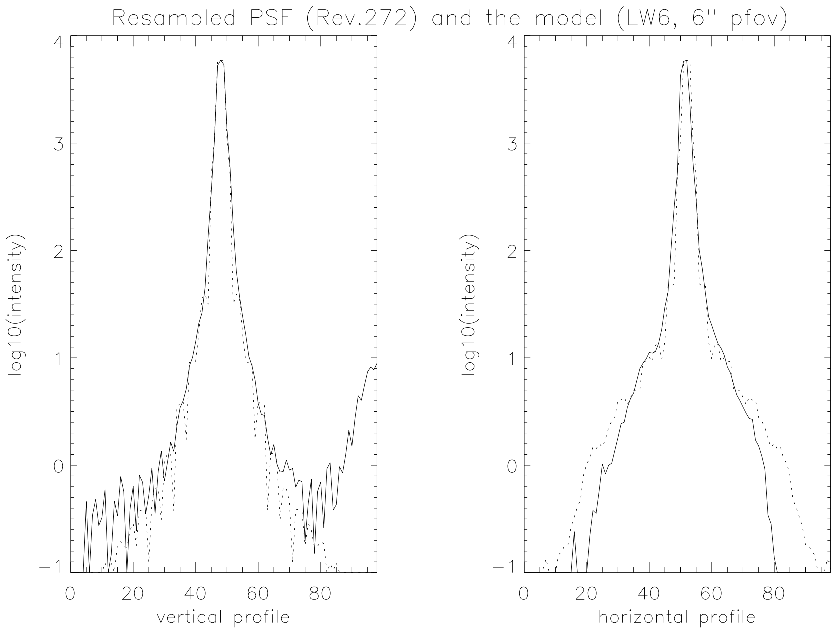

Figure 20: **Comparison of measured PSF and modelled PSF with LW6 and 6 arcsec pfov**

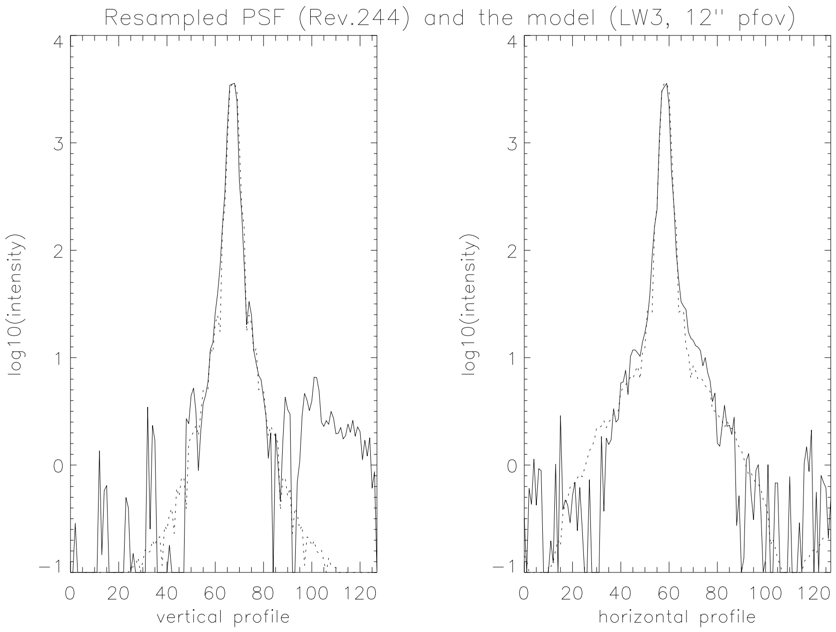

Figure 21: **Comparison of measured PSF and modelled PSF with LW3 and 12 arcsec pfov**

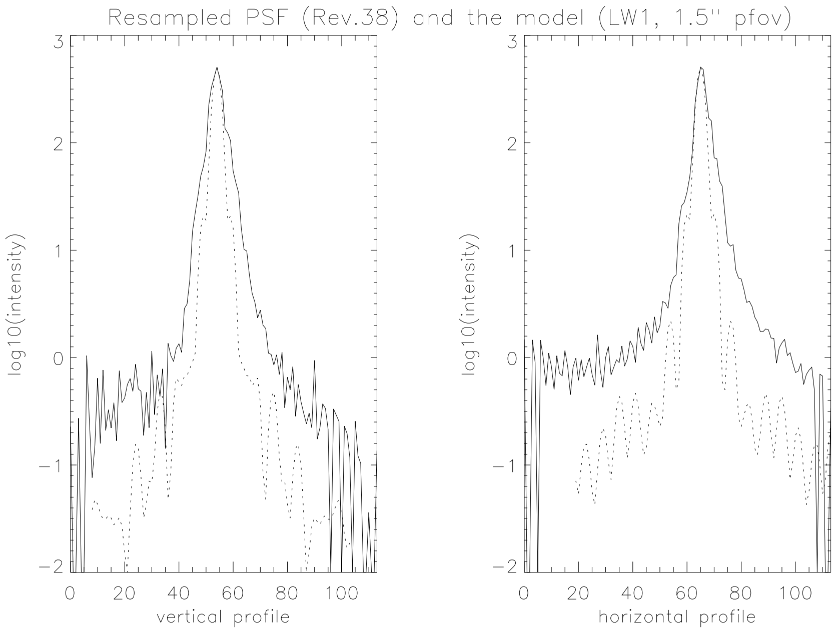

Figure 22: Comparison of measured PSF and modelled PSF with LW1 and 1.5 arcsec pfov

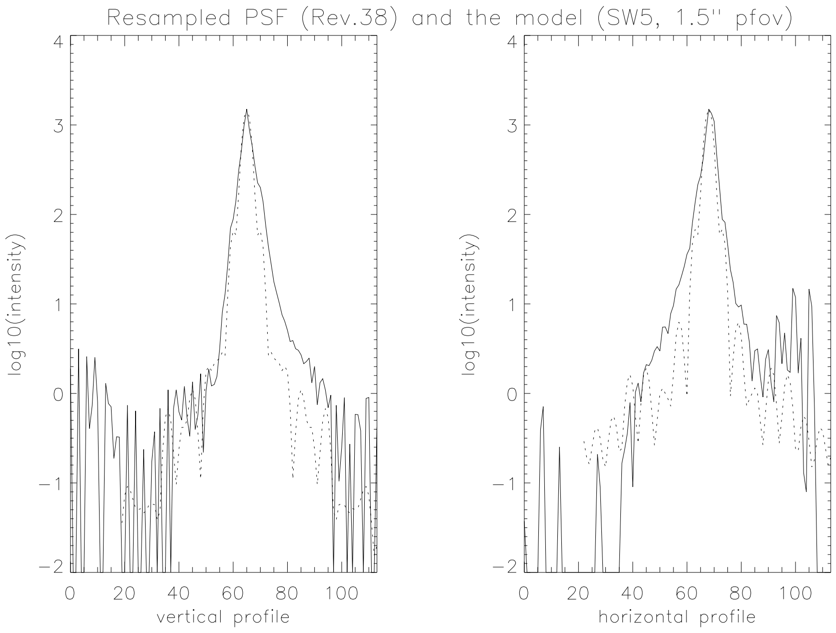

Figure 23: Comparison of measured PSF and modelled PSF with SW5 and 1.5 arcsec pfov

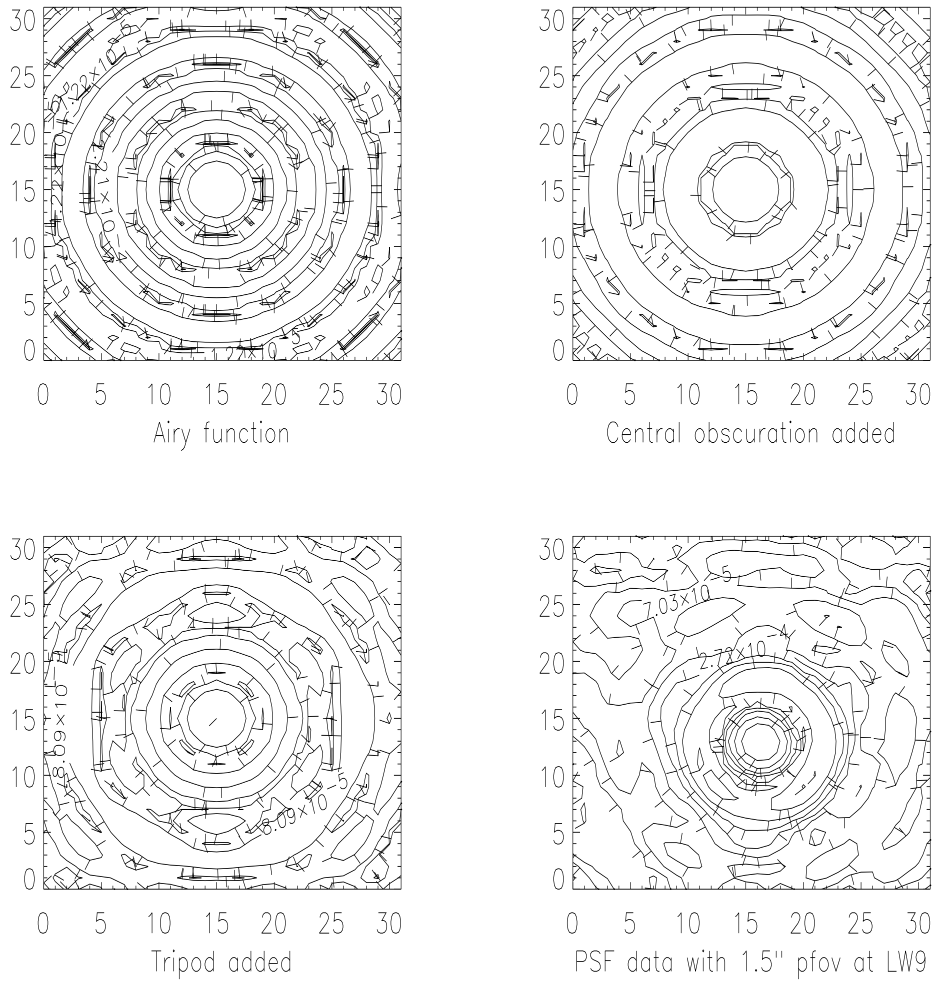

Figure 24: **Comparison with modeled PSFs for 1.5 arcsec pfov at LW9 filter.**

In the real data, the best sampled PSFs are obtained with LW9 filter using 1.5 arcsec pfov lens (see Fig. 2). These images are well compared with the PSF model. The comparison with the PSFs obtained from real data shows a very good match in the difraction ring locations as well as in the spider structure. Fig. 15 shows the horizontal and vertical profiles of a resampled PSF (0.5 arcsec sampling rate obtained by the microscan) and its corresponding PSF model. At least up to the fourth ring can be easily identified in the measured PSFs of this configuration. Fig. 24 shows contour maps of the modeled PSFs together with an example of the measured PSF image. The ticks on the contours indicate the downhill direction. The measured PSF shows even the 5th ring in the detector's corners. The central obscuration enhance the first and third ring whereas the second ring becomes very weak. When the tripod obscuration is added, the rings are modulated in a hexagonal form which is well seen in the real PSF image.

As it can be seen in Fig. 2 the PSF width of LW6 with 1.5 arcsec pfov corresponds approximately to that of LW9 with 3 arcsec pfov. Figs. 16 and 17 shows the PSF profiles for these configurations. The same comparison is possible between 3 arcsec and 6 arcsec for these filters (Figs. 18 and 19). In the same way, a PSF at LW6 with 6 arcsec pfov and that at LW3 with 12 arcsec pfov are comparable (Figs. 20 and 21). In the vertical profiles of Figs. 19, 20 and 21 an flux excess is clearly seen on the right side of the point source. This flux arises from the strongest ghost image which is especially visible with 6 and 12 arcsec lenses (see section 5.1). Its integrated flux relative to the point source flux ranges about 10 to 30% depending on the configuration and the position of the point source (see also the "Ghosts in ISOCAM images" [5]).

It is noticed that in all cases the measured PSFs show asymmetric profiles in both directions. The measured PSF in Fig. 24 shows this asymmetry in a 2D image. One can see that the intensity is higher in the top right part than the bottom left part. This assymetry is seen regardless of configuration, although the effect is more easily seen in large PSFs. The off-axis telescope field of ISOCAM does not seem to introduce such an assymetry, at least not to the extent it is seen in the real data. The origin of this assymetry is still not understood.

The PSF of LW1 filter seems to be wider than the modeled PSF (Fig. 22). But this does not seem to arise from the telescope performance, because a smaller PSF of the SW channel does not show a larger departure Fig. 23. As mentioned before, the fit of an analytical function on undersampled data gives a quite poor result. Therefore, the measurement of the PSF width using a gaussian fit is not appropriate. The full width half maximum (FWHM) has been measured in a direct way using a linear interpolation to measure the full width at the level of the half of the maximum value in the horizontal and the vertical direction on the point source. The uncertainty is estimated as the difference of the FWHM in two directions. Therefore, it should be considered as the lower limit. The measured FWHMs and the FWHM ratios of the resampled PSF with respect to their corresponding model are listed in Tab. 4. It is seen that the FWHM of LW9 with 3 arcsec pfov is quite close to that of LW6 with 1.5 arcsec pfov, such as LW9 with 6 arcsec pfov to LW6 with 3 arcsec pfov. It is noticeable that LW1 and LW10 filters show a large departure from the FWHM of their modeled PSF.

Fig. 25 shows the FWHMs of modeled PSFs as a function of the reference wavelength of the filters. The diagonal dashed line represents the diameter of the Airy disk D computed according to the approximate formula D(arcsec)= $\lambda(\mu\mathrm{m})/3$ given in the ISOCAM Observer's Manual [3]. The horizontal dashed line indicates the physical pixel size of the detector, which is the physical limit of the FWHM. The FWHMs of the modeled PSFs follow very well the Airy disc diameter except for the short wavelength PSFs (SW4 and SW5) which deviate from the computed Airy disk diameter because of the physical limit of the pixel size. The same type of plot is shown in Fig. 26 for the measured PSFs. Here the horizontal error bar indicates the bandwidth of each filter. As it was mentioned before, LW1 and LW10 show a relatively large

Table 4: Full-Width-Half-Maximum (FWHM) of the PSFs compared with the model. The first line of each filter is the FWHM in detector pixel size unit. The second line is the FWHMs ratio of the measured to the modeled PSF.

Filter (μm)	1.5" PFOV	3" PFOV	6" PFOV	12" PFOV	Average
SW1 (3.6)	-	-	-	1.004 ± 0.013	-
	-	-	-	1.003 ± 0.013	1.003 ± 0.013
SW5 (4.0)	1.104 ± 0.130	1.136 ± 0.024	1.019 ± 0.003	0.992 ± 0.007	-
	0.954 ± 0.113	1.068 ± 0.023	1.016 ± 0.005	0.990 ± 0.008	1.007 ± 0.071
LW1 (4.5)	1.531 ± 0.149	1.299 ± 0.012	1.085 ± 0.004	1.106 ± 0.050	-
	1.295 ± 0.127	1.234 ± 0.012	1.082 ± 0.004	1.104 ± 0.050	1.179 ± 0.112
LW4 (6.0)	1.384 ± 0.027	1.157 ± 0.006	1.030 ± 0.017	-	-
	0.940 ± 0.020	1.122 ± 0.006	1.007 ± 0.017	-	1.023 ± 0.077
LW2 (6.7)	1.534 ± 0.008	1.102 ± 0.008	1.025 ± 0.020	-	-
	0.945 ± 0.008	1.051 ± 0.008	0.978 ± 0.024	-	0.991 ± 0.047
LW5 (6.8)	1.599 ± 0.024	1.125 ± 0.025	1.047 ± 0.001	-	-
	0.985 ± 0.018	1.073 ± 0.024	0.999 ± 0.006	-	1.019 ± 0.043
LW6 (7.7)	1.763 ± 0.040	1.112 ± 0.007	1.056 ± 0.004	-	-
	0.974 ± 0.027	1.018 ± 0.007	0.988 ± 0.005	-	0.993 ± 0.025
LW7 (9.6)	2.126 ± 0.091	1.206 ± 0.008	1.075 ± 0.012	-	-
	0.950 ± 0.046	0.979 ± 0.007	1.030 ± 0.011	-	0.986 ± 0.043
LW8 (11.3)	2.484 ± 0.012	1.286 ± 0.043	1.064 ± 0.025	-	-
	0.943 ± 0.011	0.915 ± 0.032	1.033 ± 0.025	-	0.964 ± 0.056
LW10 (12.0)	2.204 ± 0.042	1.327 ± 0.028	1.071 ± 0.011	-	-
	0.806 ± 0.022	0.931 ± 0.020	1.039 ± 0.012	-	0.925 ± 0.097
LW3 (14.3)	3.043 ± 0.004	1.660 ± 0.004	1.076 ± 0.013	1.043 ± 0.006	-
	0.927 ± 0.008	0.972 ± 0.006	1.012 ± 0.013	1.000 ± 0.007	0.978 ± 0.034
LW9 (14.9)	3.408 ± 0.129	1.754 ± 0.026	1.112 ± 0.010	-	-
	1.001 ± 0.047	1.001 ± 0.019	1.031 ± 0.010	-	1.011 ± 0.033

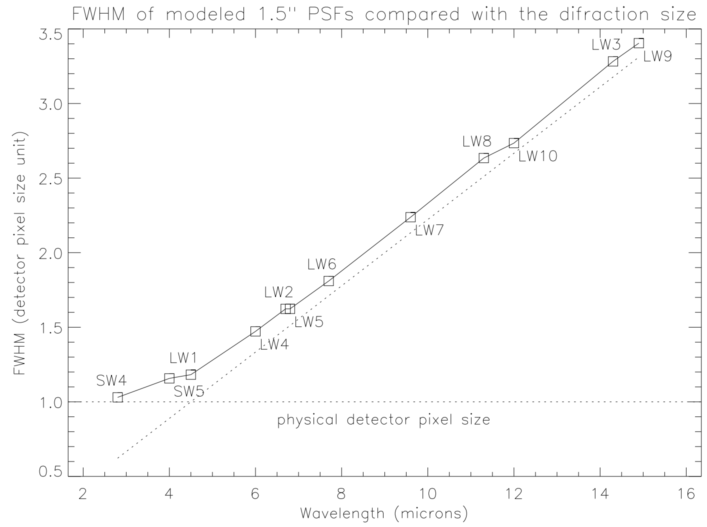

Figure 25: **FWHMs of the modeled PSFs. The dashed line is the Airy disk diameter following ISOCAM Observer's Manual.**

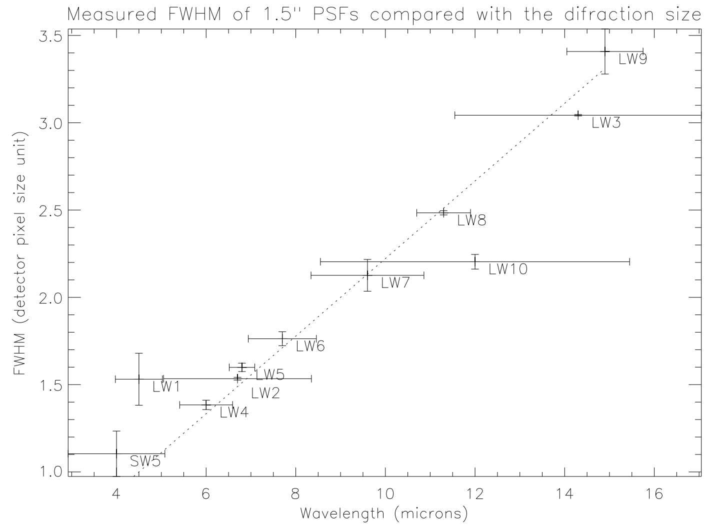

Figure 26: **FWHMs of the measured PSF. The dashed line is the Airy disk diameter following ISOCAM Observer's Manual. The horizontal error bars indicate the bandwidth of each filter.**

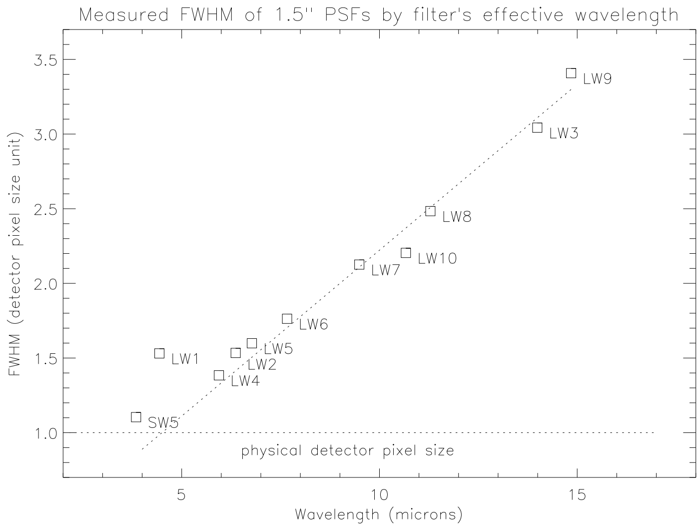

Figure 27: FWHMs of the measured PSF. The dashed line is the Airy disk diameter following ISOCAM Observer's Manual. The reference wavelength of each filter is replaced by its effective wavelength using a spectral index of -4: λ^{-4}

departure from the dashed line. Nevertheless, the departure of the filter LW10 can be explained by its large bandwidth and the spectral index estimated to be -4 for the calibration stars (Blommaert 1998 [2]). For spectra proportional to λ^{-4}, the effective wavelengths of the filters are listed in Tab. 5 If using these effective wavelength instead of the reference wavelength given in the spectra Cal-G file, Fig. 26 changes to Fig. 27. The departure of the filter LW10 is now smaller. This indicates that for filters with large bandwidth (LW10 and LW3), it is important to take into account the bandwidth effect in the modeled PSFs. In fact, the PSF integrated over the bandwidth of LW10 gives its FWHM of 2.304 ± 0.002 in pixel units. The FWHM ratio of the measured to modeled PSF is then 0.956 instead of 0.806 listed in the Tab. 4. Bandwidth integrated PSF models for a flat spectrum (λ^{-1}) can be found in the ISOCAM web page : isowww.estec.esa.nl/instr/CAM/theorpsf.html. The difference of the spectral index between -1 and -4 can give a slightly different PSF for a filter of large bandwidth. The FWHM of the flat spectrum PSF model for LW10 is 2.489 ± 0.009 and the FWHM ratio of the measured to modeled PSF is then 0.885. Therefore, one should be cautious in using the PSF models in the ISOCAM web page.

The departure of the PSF FWHM of LW1 can not be explained by the spectral contribution in the PSF. On the contrary, the spectral effect increase its departure. The cause of this LW1 PSF anomaly is not yet understood.

4.3 Flux outside the detector array and point source photometry correction factor

Using PSF models computed over larger area than the detector surface, one can estimate the fraction of flux which falls out of the detector array and derive the correction factors to recover the lost flux. The largest PSF (LW3 or LW9 with 1.5 arcsec lens) needs a correction of about 8% of the in-detector flux. Furthermore, if the background is estimated from the edge of the image, the flux loss is still larger and the correction reaches up to 11%. Tabs. 6 and 7 give the correction factors for the centered PSFs which allow to recover the flux loss. The second number of each configuration is computed for the image from which the estimated background is subtracted. If

Table 5: Effective wavelengths of the filters for the spectral index of -4

SW	$\lambda_{\rm ref}$	$\lambda_{\rm eff}$	LW	$\lambda_{\rm ref}$	$\lambda_{\rm eff}$
SW4	2.8	2.75	LW1	4.5	4.44
SW7	3.0	3.04	LW4	6.0	5.94
SW2	3.3	6.36	LW2	6.7	6.36
SW1	3.6	3.51	LW5	6.8	6.77
SW6	3.7	3.68	LW6	7.7	7.66
SW9	3.9	3.87	LW7	9.6	9.49
SW5	4.0	3.85	LW8	11.3	11.29
SW8	4.05	4.05	LW10	12.0	10.67
SW11	4.26	4.22	LW3	14.3	13.99
SW3	4.5	4.37	LW9	14.9	14.85
SW10	4.6	4.62			

Table 6: Point source flux correction factors for SW filters

Filters	1.5"	3"	6"	12"
sw1	1.014/1.026	1.000/1.000	1.000/1.000	1.000/1.000
sw2	1.009/1.021	1.000/1.000	1.000/1.000	1.000/1.000
sw3	1.022/1.034	1.000/1.014	1.000/1.000	1.000/1.000
sw4	1.004/1.020	1.000/1.000	1.000/1.000	1.000/1.000
sw5	1.020/1.031	1.000/1.015	1.000/1.000	1.000/1.000
sw6	1.014/1.026	1.000/1.000	1.000/1.000	1.000/1.000
sw7	1.009/1.022	1.000/1.000	1.000/1.000	1.000/1.000
sw8	1.016/1.028	1.000/1.000	1.000/1.000	1.000/1.000
sw9	1.015/1.028	1.000/1.000	1.000/1.000	1.000/1.000
sw10	1.023/1.037	1.000/1.012	1.000/1.000	1.000/1.000
sw11	1.020/1.031	1.000/1.015	1.000/1.000	1.000/1.000

Table 7: Point source flux correction factors for LW filters

Filters	1.5"	3"	6"	12"
lw1	1.022/1.034	1.000/1.015	1.000/1.000	1.000/1.000
lw2	1.039/1.057	1.010/1.020	1.000/1.000	1.000/1.000
lw3	1.084/1.113	1.045/1.057	1.017/1.024	1.000/1.007
lw4	1.034/1.048	1.009/1.020	1.000/1.000	1.000/1.000
lw5	1.039/1.057	1.010/1.020	1.000/1.000	1.000/1.000
lw6	1.047/1.066	1.018/1.029	1.000/1.012	1.000/1.000
lw7	1.059/1.075	1.024/1.032	1.000/1.014	1.000/1.000
lw8	1.069/1.101	1.028/1.041	1.000/1.015	1.000/1.000
lw9	1.084/1.113	1.045/1.057	1.017/1.024	1.000/1.007
lw10	1.070/1.102	1.029/1.042	1.000/1.015	1.000/1.000

Table 8: Variation of the correction factor for LW9 with 1.5" pfov (* is for background subtracted image)

position	factor	lost flux (%)	factor*	lost flux (%)*
(15.5, 15.5)	1.084	7.8	1.113	10.2
(12.0, 15.5)	1.085	7.8	1.124	11.1
(15.5, 12.0)	1.085	7.9	1.108	9.7
(12.0, 12.0)	1.086	7.9	1.113	10.2
(8.0, 15.5)	1.095	8.7	1.119	10.7
(15.5, 8.0)	1.097	8.8	1.121	10.8
(8.0, 12.0)	1.096	8.8	1.117	10.5
(12.0, 8.0)	1.098	8.9	1.125	11.1
(8.0, 8.0)	1.108	9.7	1.133	11.7
(4.0, 15.5)	1.138	12.1	1.163	14.0
(15.5, 4.0)	1.137	12.0	1.164	14.1
(4.0, 12.0)	1.140	12.2	1.162	13.9
(4.0, 8.0)	1.149	12.9	1.172	14.6
(4.0, 4.0)	1.190	15.9	1.214	17.6

the background is estimated within more inner part of the image, the correction factor may still be larger (See "ISOCAM photometry report" [2]). The correction factor depends also on the position of the point source on the dedtector and this effect is larger for big PSFs. Tab. 8 gives an idea of this dependence for 15 μm with 1.5 arcsec pfov. The fourth and fifth columns are vlaues for the background corrected image.

5 Straylight and ghost image

The same sets of data used for the in-pixel responsivity analysis are used to evaluate the contribution of diffuse straylight to the general flux level. The configurations are 12 arcsec lens at LW1 and LW3 filters. The evolution of the median value outside the field mirror may indicate this contribution because there is no fraction of the beam fallen in this area. The median value tends toward zero for the LW1 measurement for which the zodiacal emission is negligible, whereas the LW3 measurement [1] shows a regular increase over first 20 frames upto 1.5 ADU/s/gain (see Fig. 12). This corresponds to about 2% of the zodiacal emission level inside the field mirror. This suggests that a extended emission may cause an extended straylight or/and extended ghost image.

Other straylight measurements have been performed using the small Fabry mirror with 6 arcsec lens at LW9 and LW-CVF2 (LW circular variable filter 2 at 15 μm) placing a bright point source around the field mirror. A fraction of the PSF at low level is seen in the image. The median value outside the field mirror seems to correlate with the Z-axis coordinate of the source (see Figs. 28 and 29). This suggests that stray light behaves like ghost images as a function of the source position. Another possibility would be that the ghost image of the small fraction of the PSF is so extended that it influences the median value outside the field mirror. A better understanding of the ghost image is needed.

[1]This measurement was the first CAM observation in the revolution 244. The first flux level is that of the parallel mode configuration: 6 arcsec pfov at LW2 filter.

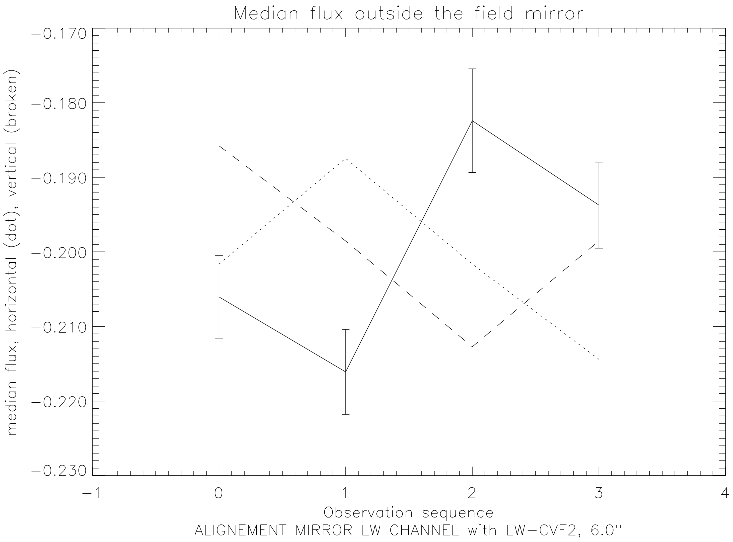

Figure 28: Median level outside the field mirror as a function of the point source position (6 arcsec pfov at CVF 15μm) in arbitrary unit

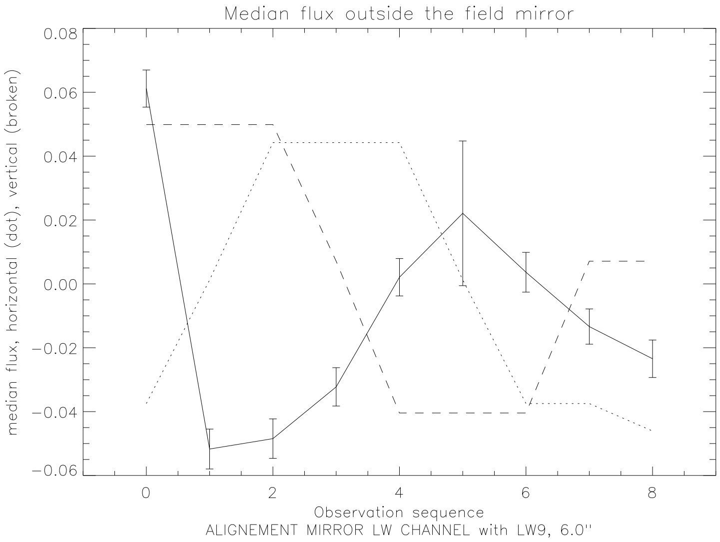

Figure 29: Median level outside the field mirror as a function of the point source position (6 arcsec pfov at LW9) in arbitrary unit

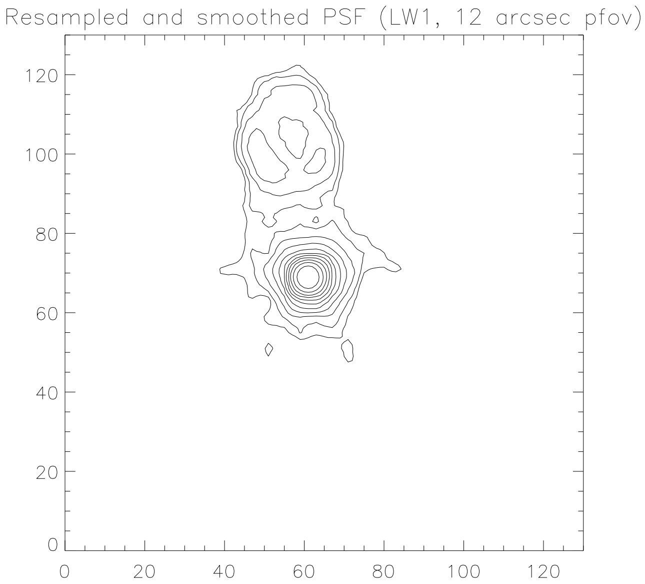

Figure 30: **Primary ghost image beside a point source (LW1 with 12 arcsec pfov)**

5.1 Ghost image on PSFs

In the PSFs of 6 arcsec pfov lens throuhg a filter, a ghost image is observed on the edge of the detector array. The similar form of ghost image is seen still better in the 12 arcsec pfov PSFs and the half of this ghost image is located outside the Fabry field morror (Fig.30) indicating that this image does not come directly from the telescope's beam. The position of the ghost image relative to the point source depends on the position of the latter and its integrated signal can reach up to 28% of that of the point source (see "Ghosts in ISOCAM images" [5]).

Theoretically, there are different types of ghost depending on the light rays in the ISOCAM. The major contribution of these ghosts arise from the reflexion on the filter. The filter was tilted to minimize this undesirable effect. However the CVF was physically impossible to be tilted. Therefore, images obtained with a CVF are most affected by ghosts. In order to investigate the

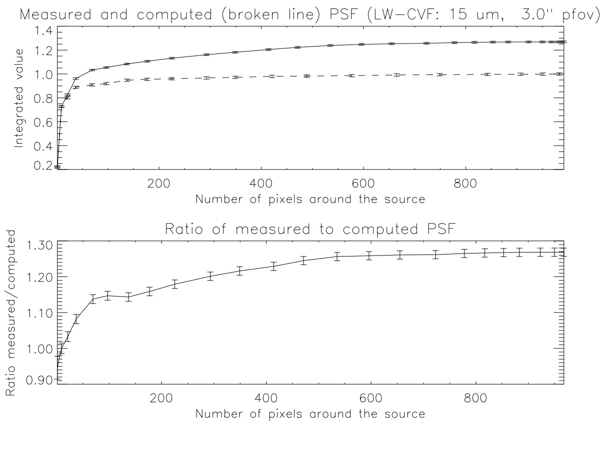

Figure 31: **Comparison between CVF data at 15 μm with 3 arcsec pfov and the computed PSF**

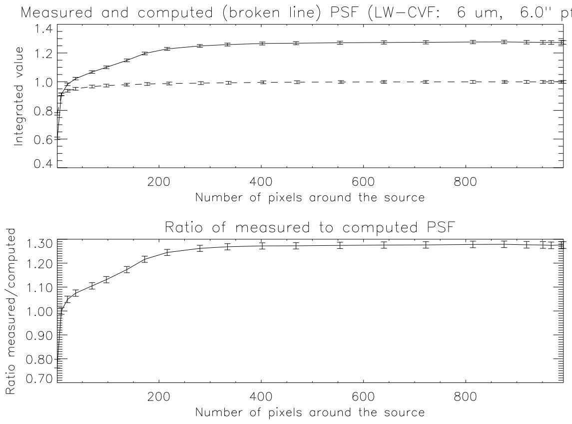

Figure 32: **Comparison between CVF data at 6 μm with 6 arcsec pfov and the computed PSF**

ghost behaviour, some additional observations have been made as a part of the routine phase calibration using CVFs.

Here we examine the PSF observations performed using CVFs (see Tab. 3). Figs. 31 and 32 show point source integration curves. These two examples are taken to show a relatively large PSF (at 15 μm with 3 arcsec pfov) and a small PSF (at 6 μm with 6 arcsec pfov). Here the curve of the rising flux is normalised to the computed PSF in the small region of the maximum flux (the extreme left in the Figures). This way, it is shown clearly that the flux excess is caused by an extended structure, which is a ghost. Despite the very different case of Figs. 31 and 32, the contribution of the ghost to the flux seems very similar. The lower figure of each case shows clearly a contribution of about 28%. This value is obtained independently using CVF data of different pfov (see aloso Biviano et al. [1]).

These ghost images are of the same kind as that seen in Fig. 30, although in this case the ghost falls beside the point source because of the filter tilt. With a CVF, which is not tilted, the ghost falls right on the point source whatever its position is. A simple optical model can show approximately where the ghost image falls for different positions of point source (Fig. 33). This type of ghost is caused by the reflexions on the detector plane and on the filter plane (Fig. 34).

6 Pointing jitter and deconvolution

For most of the configurations the ISOCAM's pixel size is not small enough to obtain a sufficient sampling with respect to the PSF size. Only LW3, LW7, LW8, LW9 and LW10 filters with 1.5 arcsec pfov lens can provide a correctly sampled image unless making a micro scanned image (see Figs. 1 and 2). However, the deconvolution turns out not to be trivial even for correctly sampled images. The difficulty in applying a deconvolution processing on a well sampled ISOCAM data may arise from the pointing jitter and the transient effect.

The jitter information in IIPH (Instantaneous Instrument Pointing History) might be used for the instantanious point source position, but the estimation of the jitter using a gaussian fit applied on each frame does not match at all the pointing offset given in IIPH file. This information is considered for now not to be usable for the correction of the pointing jitter. The jitter could be measured by evaluating a point source position in each frame. The difficulty arises from glitches and de-glitching routines. On one hand, any de-glitching routine may mask very often the brightest pixel because it has a similar behaviour as a glitch precisely due to

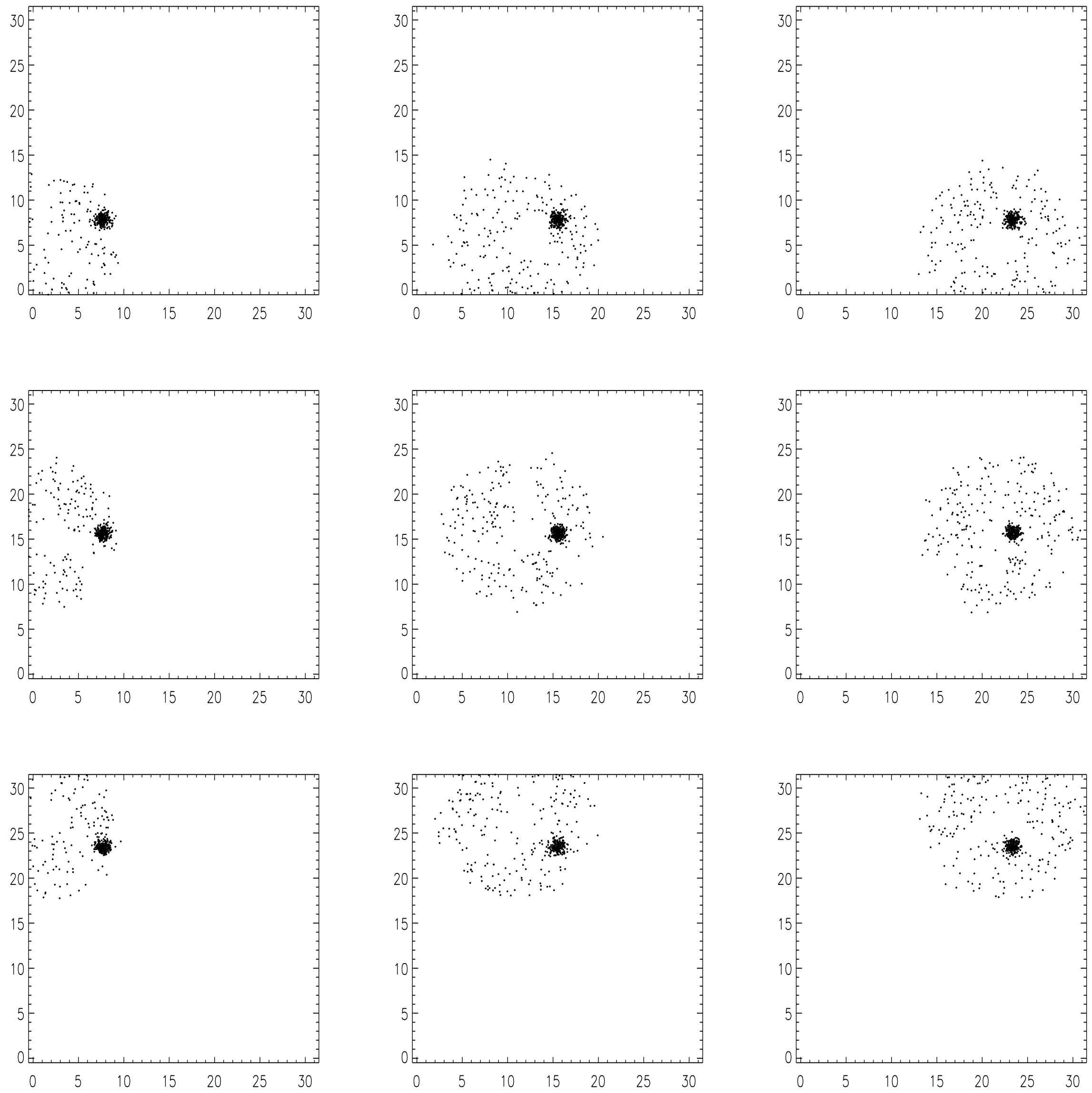

Figure 33: Simulated ghost for a CVF at 15 μm and 6 arcsec pfov with a point source at different positions

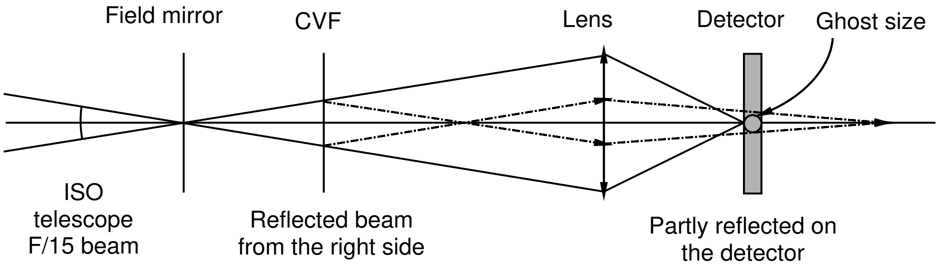

Figure 34: A fraction of the converging beam from a point source is reflected on the detector and comes back onto it after passing through the lens, reflecting on the filter and passing again through the lens.

the pointing jitter. On the other hand, glitches make impossible the systematical automatic determination of the source position in each frame. The practical solution for this may be to estimate the point source position only in a small area centered on the source reducing the number of glitches inside it.

6.1 PSF fit for the pointing jitter estimation

The position of a point source in a image can be determined by fitting a set of theoretical PSFs. This method is "theoretically" more accurate than any other method, but it certainly is not allmighty which gives an exact result in any case. A set of simulations have been performed to assess the reliability of this PSF fit method.

A set of PSFs are computed for use of fit onto a point source image. In our example, there are $11 \times 11 = 121$ PSFs, which allow to determine the position of the point source up to an accuracy of $1/11$ of the pixel size. For the sake of clarity a short wavelength giving a small PSF has been chosen, because the worse the spatial sampling rate is, the less accurate is the determination of the point source position with other methods. This is shown in Figs. 35 to 37. The crosses are the real positions of the 121 PSFs and the squares are their positions determined by gaussian fit algorithm. It is clearly seen that the computed positions in this way are biased towards the pixel center and this trend is more significant for badly sampled images. Although the computed PSFs are free of noise except for the mathematical noise, the effect of the bad sampling is well seen. In Figs. 36 and 37 this trend is seen not in a uniform way but rather in a discontinuous way. This is due to the different form of the gaussian relative to the PSF. This difference comes on one hand from the difference between the gaussian and the optical PSF, on the other hand from the convolution effect of pixel size on the optical PSF. The discontinuous aspect in Figs. 36 and 37 reveals this second effect, because the convolution effect is dominant when the pixel size is large compared to the optical PSF width.

If a PSF fit is used on these data, then the exact positions are found, which is quite obvious because we are fitting a function to itself and the error is null as long as the data are noise free. However this exact matching is no longer obtained as soon as a noise is introduced on the data. When working on real data the situation is still worse because of the difference between the computed and real PSFs which is, in principle, always existing because there are

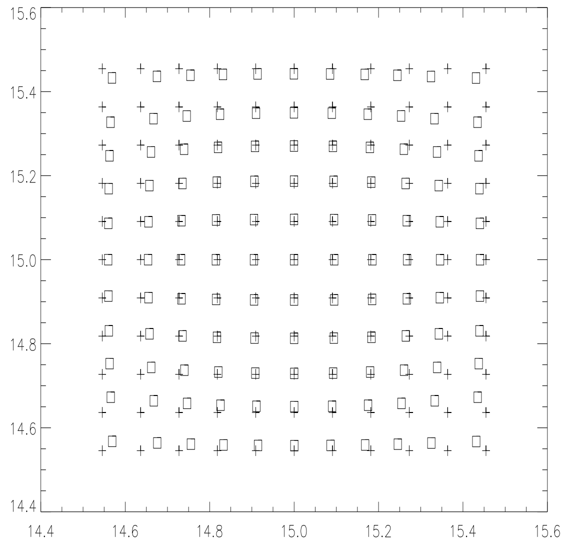

Figure 35: **Positions of LW1 PSF with 1.5 arcsec pfov determined by gaussian fit routine**

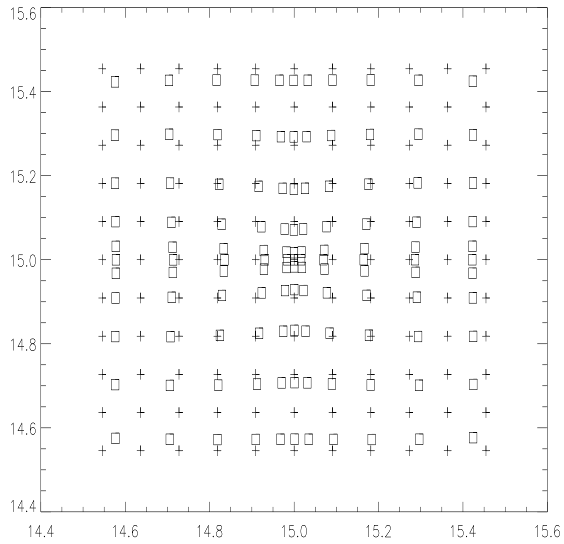

Figure 36: **Positions of LW1 PSF with 3 arcsec pfov determined by gaussian fit routine**

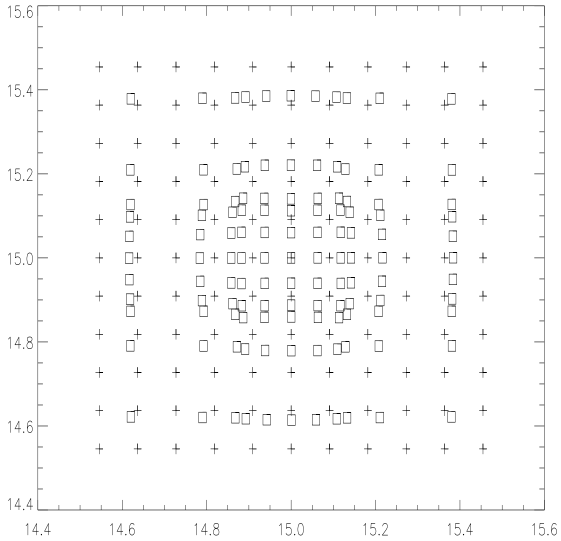

Figure 37: Positions of LW1 PSF with 6 arcsec pfov determined by gaussian fit routine

Table 9: Statistics of the 100 trials for LW1 with 1.5 arcsec pfov

signal/noise	detection (%)	maximum offset (pixel unit)
3.0	3.00	1.02
10.0	25.00	0.91
50.0	93.00	0.09
100.0	100.00	0.00
200.0	100.00	0.00
300.0	100.00	0.00

always unpredictable elements on the real PSF such as the pointing jitter of the telescope and any instrumental secondary effect which are not taken into account in the PSF computations. Bearing this fact in mind a set of simulations has been performed. Obviously the accuracy of the PSF fit depends on the signal to noise ratio on the data, especially on those of the pixels surrounding the brightest pixel. This means that the fit accuracy depends on the PSF size, so on the filter and the lens used for the observation.

One trial of the simulation consists of creating an observation data and apply the PSF fit algorithm and compute the accuracy of the result. To create an observation we first select randomly one image out of the computed PSF set and add the noise of a chosen signal to noise ratio and multiply it by an uniformly distributed random factor between 0 and 1000. Some trials are made for a fixed configuration (PSF size) and a fixed signal to noise ratio to obtain statistics on the accuracy of the PSF fit algorithm. Then this trials are repeated for different signal to noise ratio. A set of statistics obtained in this way gives an idea of the accuracy achieved by using the PSF fit algorithm as a function of the PSF size and the signal to noise ratio of the brightest pixel.

The statistics are shown in Tabs. 9 to 11 for simulated observations at LW1 with 3 lenses (1.5, 3, 6 arcsec pfovs). Figs. 38 to 40 show the distribution of errors for the corresponding trials.

Table 10: Statistics of the 100 trials for LW1 with 3 arcsec pfov

signal/noise	detection (%)	maximum offset (pixel unit)
3.0	2.00	0.98
10.0	23.00	0.71
50.0	70.00	0.29
100.0	77.00	0.20
200.0	96.00	0.09
300.0	99.00	0.09

Table 11: Statistics of the 100 trials for LW1 with 6 arcsec pfov

signal/noise	detection (%)	maximum offset (pixel unit)
3.0	3.00	1.22
10.0	14.00	0.73
50.0	37.00	0.37
100.0	78.00	0.18
200.0	96.00	0.09
300.0	100.00	0.00

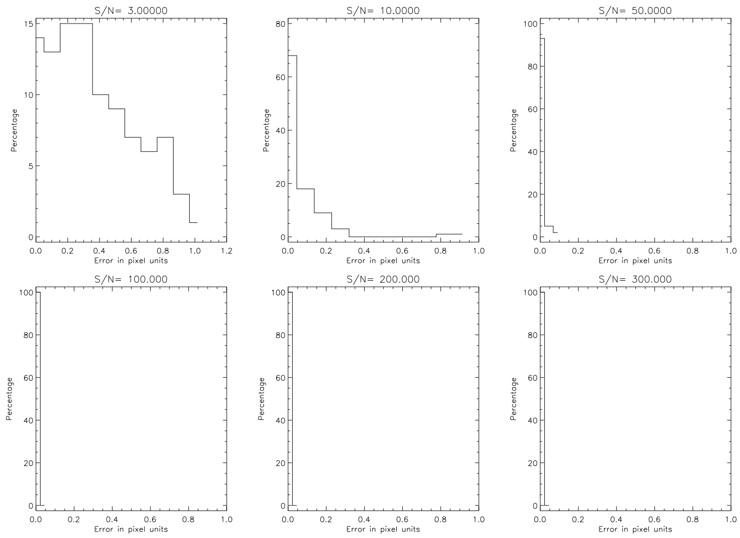

Figure 38: Histograms of error on the determined point source position of 1.5 arcsec pfov data over 100 trials

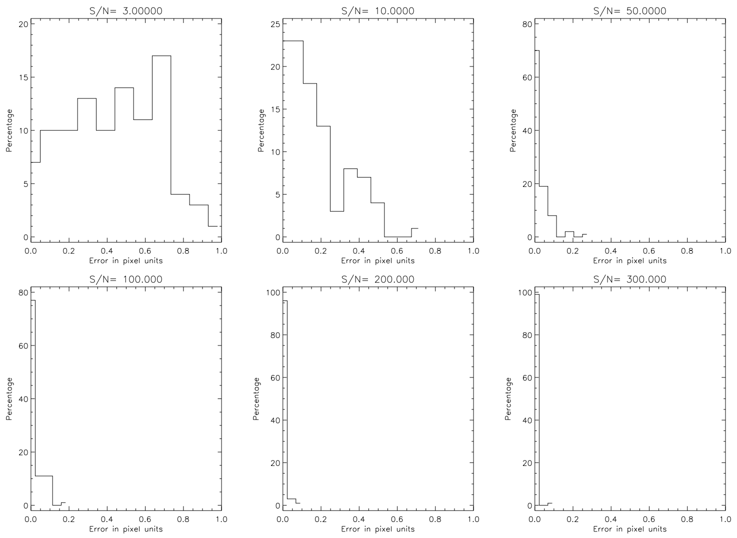

Figure 39: Histograms of error on the determined point source position of 3 arcsec pfov data over 100 trials

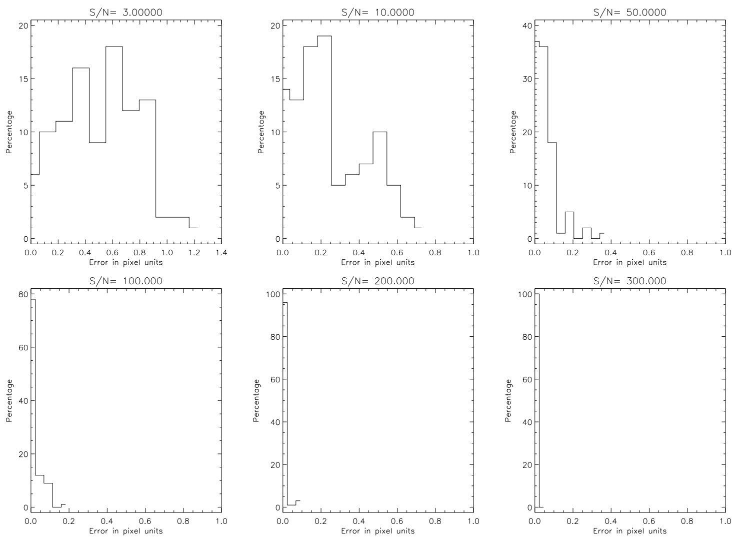

Figure 40: Histograms of error on the determined point source position of 6 arcsec pfov data over 100 trials

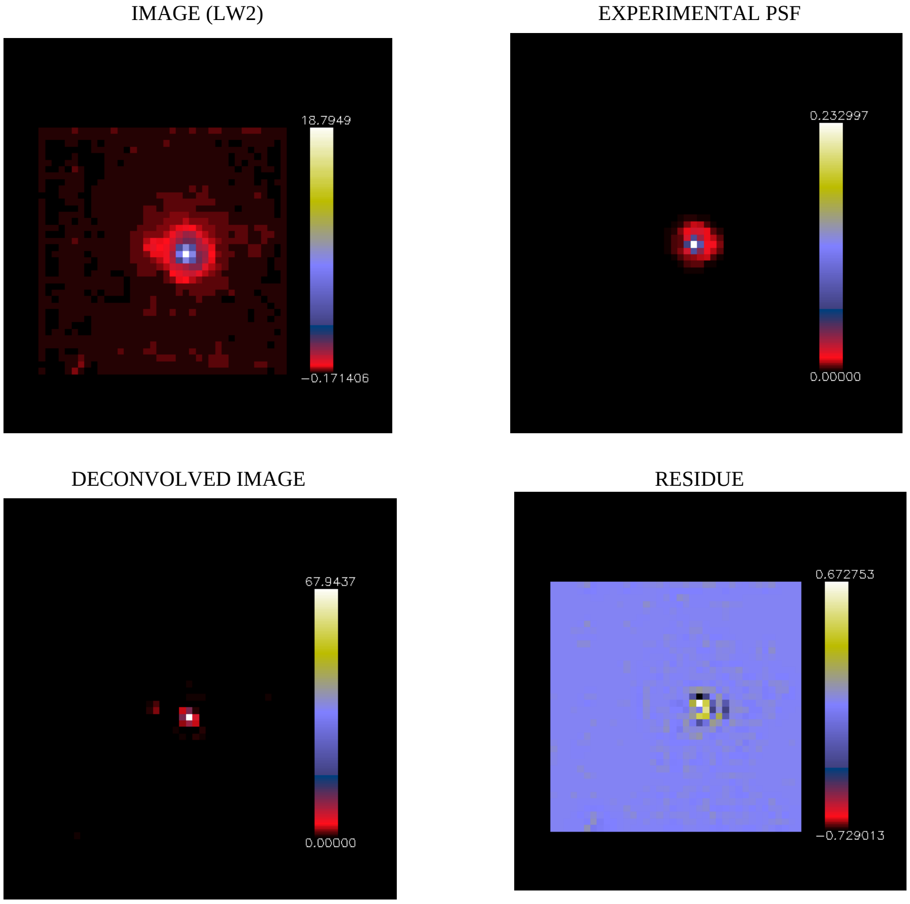

Figure 41: "Deconvolution" of a ISOCAM image in O.Laurent et al. 1998

In the worst case of Tab. 11, *i.e.* with the filter of the shortest wavelength and 6 arcsec pfov lens, it is seen that a signal to noise ratio of at least 300 is needed to obtain a 100% accuracy.

6.2 Deconvolution of the ISOCAM image

As mentioned before the number of configurations which give a correct spatial sampling rate is very limited unless doing a microscanning. Nevertheless, some tentatives have been made to deconvolve ISOCAM images (see O.Laurent et al. [4]). After correcting for the pointing jitter estimated by a fitting method, one can produce a "jitter free" final image. However, trying to deconvolve this image using a PSF turns out to give still a poor result, probably due to the transient effect. The way adopted by O.Laurent to minimise this effect is to search for one frame out of the whole PSF measurement of the corresponding configuration which fits best the source one wants to "deconvolve" (Fig. 41). Obviously, this method is applicable only if the source is point-like. Apparently, the selection of a specific PSF allows to "deconvolve" even under-sampled data (LW2 with 1.5 arcsec pfov in this example), but this means that this "deconvolution" is a source dependent procedure, implying as many number of "deconvolutions" as that of sources which, in addition, should have a suffucent signal to noise to fit reasonably a PSF. Therefore, this "deconvolution" method is only applicable to some very specific cases.

In the actual status, even for the most favorable sampling configuration there is no simple method applicable to any data without any specific consideration.

References

[1] A. Biviano, B. Altieri., J. Blommaert, F. Boulanger, D. Cesarsky, K. Okumura, W. Reach Topics in ISOCAM Spectroscopy Calibration. Procedings first ISO workshop on analytical spectroscopy, 1997.

[2] J. Blommaert. ISOCAM photometry report. 1998.

[3] ISOCAM Observer's Manual. ESA, 1994.

[4] O. Laurent et al. ISOCAM observation of the ultraluminous galaxies IRAS19254-7245, IRAS23128-5919 and IRAS14348-1447. in preparation, 1998.

[5] K. Okumura. Ghosts in ISOCAM images. 1998.